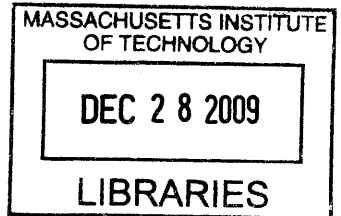


**Passive aeroelastic tailoring of wind turbine blades
- A numerical analysis -**

by

Christian Deilmann

Dipl.-Ing. Mechanical Engineering and Management
Technische Universität München, 2008



SUBMITTED TO THE DEPARTMENT OF MECHANICAL ENGINEERING IN PARTIAL
FULFILLMENT OF THE REQUIREMENTS FOR THE DEGREE OF

MASTER OF SCIENCE IN MECHANICAL ENGINEERING
AT THE

MASSACHUSETTS INSTITUTE OF TECHNOLOGY

SEPTEMBER 2009

ARCHIVES

© 2009 Christian Deilmann. All rights reserved.

The author hereby grants to MIT permission to reproduce
and to distribute publicly paper and electronic
copies of this thesis document in whole or in part
in any medium now known or hereafter created.


Signature of Author.....

Department of Mechanical Engineering
August 10, 2009

Certified by.....

Klaus-Jürgen Bathe
Professor of Mechanical Engineering
Thesis Advisor

Accepted by.....


.....
David E. Hardt
Professor of Mechanical Engineering
Chairman, Committee for Graduate Students

Passive aeroelastic tailoring of wind turbine blades - A numerical analysis -

by

Christian Deilmann

Submitted to the Department of Mechanical Engineering
on August 18th, 2009 in Partial Fulfillment of the
Requirements for the Degree of
Master of Science in Mechanical Engineering

Abstract

This research aims to have an impact towards a sustainable energy supply. In wind power generation losses occur at tip speed ratios which the rotor was not designed for. Since the ideal blade shape changes nonlinearly with rising wind speeds currently used pitch control mechanisms can only approach the ideal blade deformation.

However aeroelastic effects, which cause additional deformation, are almost unavoidable in flexible blade design and it is desirable to tailor these effects to our advantage by a controlled use of orthotropic material properties and a smart design of the blade structure.

The idea of systematic aeroelastic tailoring is not new but research has not yet solved the design challenge partly due to the lack of accurate simulation tools.

Passively adaptive rotor blades would enable systematic aeroelastic tailoring and have the potential to reduce the cost of energy by around 6% [1].

Within this thesis a design procedure for passively adaptive rotor blades has been developed. It consists of an aerodynamic simulation and optimization code (based on Blade Element Momentum Theory), a structural simulation (based on Finite Element Analysis) and a fluid structure interaction correction loop (based on CFD and FEM).

Using the developed design code passively adaptive rotor blades have been designed for the NREL phase VI test turbine. The results show that an ideal passively adaptive blade could improve the efficiency of the test turbine by 3% to 6%. The proposed rotor designs can only approach these improvements. However they do improve the efficiency and since the design only requires a precisely calculated stacking of composite material layers, the cost for manufacturing will not increase significantly.

This work is a contribution to solve the design challenge of passively adaptive rotor blades and further research may be based on it.

Thesis Advisor: Klaus-Jürgen Bathe.
Title: Professor of Mechanical Engineering

Acknowledgements

First and foremost, I would like to thank my thesis advisor Professor Klaus-Jürgen Bathe for his great effort in guidance, constructive criticism, and excellent teaching. His comprehensive knowledge in engineering and his ability to motivate and encourage his students are unique. He is a great inspiration and I am most grateful to have had the opportunity to work with him.

Furthermore, I would like to thank Prof. K. Horstmann (Deutsches Zentrum für Luft- und Raumfahrt), Mr. J. Johansen (RISOE Institute) and Mr. F. Rasmussen (RISOE Institute) for their extensive discussions on wind turbine theory.

For allowing me to use their computational codes, I would like to thank ADINA R&D, Inc., the National Laboratory for Renewable Energies, Prof. H. Funke (University of Dortmund) and Prof. M. Drela (Massachusetts Institute of Technology).

Finally, I would like to mention and thank my colleagues at the Finite Element Research Laboratory, Do-Nyun Kim, Reza Sharifi Sedeh, Jared Ahern, Haining Zheng, Tianyun Liu, Ofer Aharon, Jing-Zhong Xie and Joris Degroote for their great support and the friendly and inspiring working atmosphere.

Table of content

1. Introduction	6
1.1. Obtaining a sustainable energy supply	6
1.2. Aeroelastic tailoring of wind turbine blades	7
2. The wind turbine	9
2.1. Theoretical wind power potential.....	10
2.1.1. Momentum theory	11
2.1.2. Momentum theory including wake rotation	13
2.2. Wind turbine aerodynamics	16
2.2.1. Airfoils	16
2.2.2. Blade element theory.....	18
2.2.3. Blade element momentum theory	20
2.2.4. Iterative solution method of the BEMT	20
3. Rotor design and simulation.....	22
3.1. Rotor design procedure based on BEMT	22
3.2. Computational aerodynamic simulation of wind turbines	24
3.3. Comparison of simulation programs	26
4. Analysis of wind turbine optimization possibilities.....	27
4.1. Loss factors in steady state operation.....	27
4.2. Passively adaptive wind turbine blades.....	28
5. A numerical procedure for the design of passively adaptive turbine blades	31
5.1. Aerodynamic simulation	33
5.2. Structural response simulation	34
5.3. Structural and material design.....	35
5.4. FSI coupling	38
6. Airfoil analysis	39
6.1. The S809 airfoil.....	39
6.2. CFD simulations.....	40
6.2.1. CFD Model, boundary conditions and loading	40
6.2.2. The CFD results	41

6.3. Panel code simulations	45
6.4. Processing a 360° dataset of airfoil characteristics	47
7. The NREL phase VI test turbine	48
7.1. Turbine design and characteristics	48
7.2. Model construction for simulations.....	49
7.3. Verification of aerodynamic simulation results	51
8. Aeroelastic tailoring to optimize the NREL test turbine	52
8.1. Aerodynamic optimization of the blade profile	52
8.1.1. Potential power enhancement.....	52
8.1.2. Optimal blade deformation.....	53
8.1.3. Aerodynamic loading	56
8.2. Structural simulation of blade profile deformations	57
8.2.1. Material design	57
8.2.2. Structural design and simulation	59
8.2.2.1. Constant shell thickness	59
8.2.2.2. Investigation of structural design effects.....	62
8.2.2.3. Optimization of the structure.....	64
8.3. Analysis of FSI coupling effects	66
8.3.1. The 2D model of a blade cross-section	66
8.3.2. Stiffness properties	67
8.3.3. FSI analysis	70
8.4. Discussion of the results.....	71
9. Conclusion and outlook	72
Appendix A. Comparison of wind turbine simulation codes	74
References	75

1. Introduction

1.1. Obtaining a sustainable energy supply

The current worldwide energy system¹ depends to 85% on carbon-based fossil fuels [2], which provide the least expensive and most convenient options for energy conversion into useful applications. However, these resources are limited and are environmentally unsustainable. Converting the current fossil fuel based energy systems into sustainable systems presents a great challenge, but climate change and energy market forces are major driving factors. For a successful change, efforts in policy, technology, finance and public acceptance have to be aligned. The currently observed sense of urgency is much influenced by impending consequences in global climate change, but the uncertainty of climate change policy [3] leads utility companies to delay new plant decisions. Power plants, expected to be built in the next two decades, will comprise about 50% of the total generation capacity by the end of that period [4]. In addition, a number of new technologies are emerging, but they have not yet proven to be profitable. The choice of the design of the future energy system is now wide open but will be much narrower by 2020 [5]. These circumstances, that is, uncertainty in policy, uncertainty in promising technology, high demand for new energy system capacities, and the long term obligations, lead to major challenges in decision-making for future energy systems.

The holistic method to design an optimized energy scenario and quantitatively evaluate promising technologies for implementation [6] reveals energy paths to the future, which follow the principles of scientific optimization and sustainability.

Since research endeavors and legislation affect free market decisions within the energy system, the developed method [6] aims at guiding researchers and politicians to make most effective decisions in contributing to a sustainable energy system.

¹*The expression “energy system” is defined in this paper as a set of interacting energy conversion- and application components. An important characterization is the total input-/ output quantity beyond its boundaries. The boundaries can encompass one component (e.g. power plant, car, etc.) up to a worldwide consideration of the sum of all components.*

1.2. Aeroelastic tailoring of wind turbine blades

Aeroelastic tailoring of wind turbine blades by designing passively adaptive rotors turns out to be a promising research project with a high contribution potential towards a sustainable energy supply. The concept to adapt wind turbine rotor blades passively by using non-isotropic material characteristics which induce a deformation due to changing loads is not new. However, it has not yet been applied in commercial wind turbines and research has not yet solved the design challenge, partly due to the lack of accurate simulation tools.

The thesis begins with a summary of wind turbine theory to review knowledge in order to analyze wind turbine optimization potential and to develop procedures for rotor blade simulations.

An assessment of computational aerodynamic codes for wind turbines has been performed as a preceding step to the development of a numerical procedure for the design of passively adaptive rotor blades.

The proposed procedure combines an aerodynamic simulation (based on BEMT, i.e. Blade Element Momentum Theory) and a structural dynamic simulation (based on Finite Element Analysis) in order to simulate the structural response of the blade due to changing loads as a result of different turbine operations. In a fluid structure interaction assessment the coupling effects of the blade deformation and changes in loading are being examined and considered in the design procedure with a FSI correction loop.

An essential requirement for the aerodynamic simulation in the BEMT method is an extensive and accurate set of airfoil characteristics. These are generated and validated by a panel code as well as a CFD code. The CFD validation is also necessary for the assessment of the coupling effects within the FSI analysis.

In the final section of the thesis, the test turbine (phase VI) of the U.S. National Laboratory for Renewable Energy has been modeled and passively adaptive blades have been designed using the proposed design procedure. The result of aerodynamic simulation shows that optimal adaptive rotor blades have the potential to improve the efficiency of the phase VI turbine by 3% to 6%.

The structural response simulation reveals how different material characteristics effect blade deformation. Passively adaptive rotor blades, built out of orthotropic composite materials, have the ability to improve energy efficiency of the phase VI turbine.

Since the production of passively adaptive blades only requires a precisely calculated stacking of composite material layers, the costs for manufacturing will not increase significantly. Hence, if research has solved the design challenge of passively adaptive blades, the technology will most likely find applications in commercial wind turbines.

2. The wind turbine

Wind turbines are energy conversion devices used to harness the power of wind for electricity generation. The primary component of a wind turbine is the rotor. The rotor transforms the kinetic energy of moving air into mechanical energy, which is then converted into electricity. The ability of the rotor to convert a maximum proportion of wind energy flowing through the swept area into mechanical energy is a direct result of its aerodynamic properties.

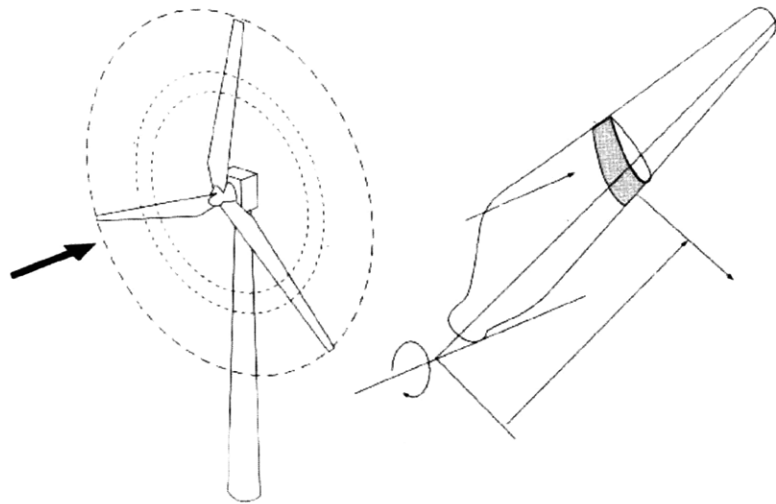


Fig. 1: Basic concept of a horizontal axis wind turbine [7]

Fig. 1 schematically shows a horizontal axis wind turbine with the wind direction perpendicular to the swept area. In earlier times, wind turbines used the drag of the wind to create driving torque. Today's lift machines have airfoil shaped blades to make use of aerodynamic lift, which results in much higher power coefficients in comparison to drag devices.

Wind turbines are designed to produce electricity at the lowest costs. This implies high efficiency, low production and maintenance costs and high durability. In order to achieve the best overall result, tradeoffs are sometimes necessary. To ensure optimal efficiencies and to control wind turbines to keep material stresses in a certain range, the turbine should be able to control rotational speed and the angle of airflow attack on its rotor blades. Incorporating such possibilities by adding more complex gearboxes and blade pitch control systems results in more expensive devices and is only profitable for large wind turbines. Small wind turbines are often

fixed speed machines and control maximum loading passively by using stall mechanisms which occur at high wind speeds.

Fig. 2 shows a typical average annual wind power density curve and the minimum as well as maximum operating wind speed for wind turbines. It can be seen that almost all of the annual power density is captured between the minimum and maximum turbine limits.

An ideal power curve for a wind turbine (Fig. 3) starts in Phase I at the minimum wind speed, V_{min} , and follows a cubic parabola due to the exponent in the formula of kinetic energy for wind. At the rated wind speed, V_N , the turbine starts to reduce the power efficiency of the rotor in order to keep material loads low (Phase III). The transition between the operating ranges is marked by phase II. The ideal power curve of Phase I can, however hardly be achieved in practice as the construction of an ideal rotor is not feasible.

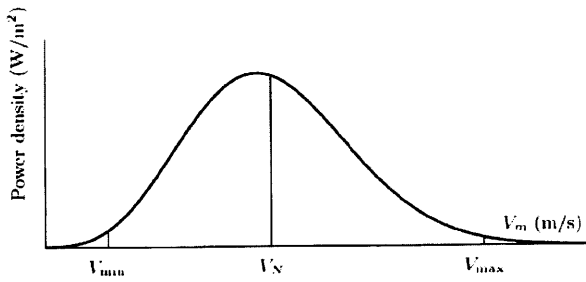


Fig. 2: Typical power density over wind speed [8]

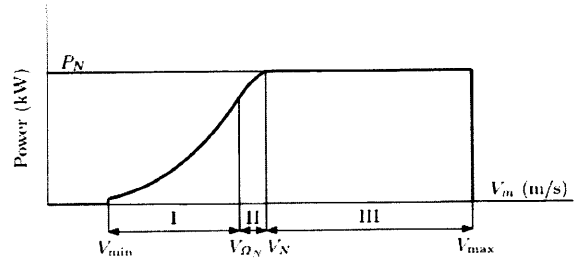


Fig. 3: Major phases of turbine operation [8]

2.1. Theoretical wind power potential

The kinetic energy per unit time (P_v) that passes through the area of a wind turbine depends on the mass flow of air, \dot{m} , and the airflow speed, V , (Eq. 2.1).

$$P_v = \frac{1}{2} \dot{m} V^2 = \frac{1}{2} \rho A V^3 \quad (2.1)$$

But this power is not available due to losses, and the fact that the air needs residual velocity to move from the turbine outlet.

2.1.1. Momentum theory

Alfred Betz created the actuator disc model based on axial momentum theory to investigate the optimal power extraction of a wind conversion system. It basically shows the optimal relationship between the wind speed in front and behind the turbine.

In the model, the turbine is regarded as an actuator disc. It assumes infinite rotor speed, no wake rotation, no swirl and no drag. The disc model is not limited by the laws of fluid mechanics. Since the actuator disc extracts part of the kinetic energy of the wind, the upstream wind speed, V , is necessarily greater than the downstream wind speed, $V_{-\infty}$. The wind speed at the turbine has a value between the upstream- and the downstream velocity.

Consequently this has an impact on the cross-sectional areas before the disc, A_{∞} , at the disc, A_D , and behind the disc, $A_{-\infty}$, since the mass flow rate has to be the same everywhere (Eq. 2.2). Fig 4 and 5 as well as Eq. 2.2 show these physical relations where ρ is the mass density and V_D the air flow speed at the disc.

$$\rho A_{\infty} V = \rho A_D V_D = \rho A_{-\infty} V_{-\infty} \quad (2.2)$$

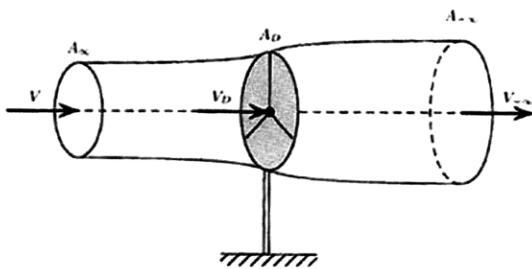


Fig. 4: Airflow through an actuator disc [8]

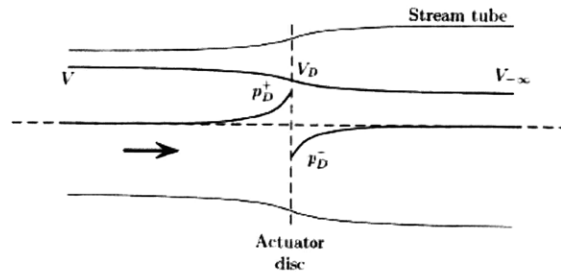


Fig. 5: Air speed and pressure in stream tube [8]

Due to conservation of mass the velocity slightly before and behind the disc stays the same. The thrust force, T_D , at the actuator disc is proportional to the pressure drop slightly upstream and downstream of the turbine. Due to Bernoulli's laws the force is proportional to the wind speed drop far upstream and far downstream of the turbine (Eq 2.3).

$$T_D = (p_D^+ - p_D^-)A_D = (V - V_{-\infty})\rho A_D V_D \quad (2.3)$$

The axial flow interference factor, a , describes the axial induction ratio as a fractional decrease in wind velocity between the free-stream and the rotor plane (Eq. 2.4).

$$a = \frac{V - V_D}{V} \quad V_D = V(1 - a) \quad (2.4)$$

By applying Bernoulli's equation (which states that, under uniform conditions, the total energy of the flow remains constant provided no work is done on the fluid) before and after the disc and equating these, Eq. 2.5 is obtained [8].

$$V_{-\infty} = V(1 - 2a) \quad (2.5)$$

It turns out that the momentum theory applies up to $a = 0.5$. Equation 2.5 shows that $V_{-\infty}$ will be negative for values of $a > 0.5$, which is physically not possible [7]. Flow field characteristics are not necessarily constant over the disc radius, r . For this reason the actuator disc will be segmented into several annular areas to perform calculations individually for each segment. Using Eq. 2.3 and 2.4, the incremental thrust force is introduced by Eq. 2.6. The resulting power harnessed by the actuator disc (assuming a constant airflow speed and induction ratio) is given by Eq. 2.7.

$$dT_D = 4a(1 - a)\rho V^2 \pi r dr \quad (2.6)$$

$$P_D = T_D V_D = 2\rho A_D V^3 a(1 - a)^2 \quad (2.7)$$

The power coefficient is given by Eq. 2.8 using Eq. 2.1 and Eq. 2.7.

$$C_P = \frac{P_D}{P_V} = 4a(1 - a)^2 \quad (2.8)$$

The maximum theoretical efficiency (known as the Betz Limit) is $C_{P_{\max}} = 0.593$ and occurs for a factor $a = 1/3$. This upper-boundary applies for any type of wind turbine. Modern wind turbines achieve power coefficients of about 0.45 in practice.

2.1.2. Momentum theory including wake rotation

In the previous analysis, it was assumed that no rotation was imparted to the flow. The theory can be extended to the case where the rotation of the rotor generates angular momentum. The exertion of a torque on the rotor disc requires an equal opposite torque to be imposed upon the air. The consequence of this reaction torque is to cause the air to rotate in a direction opposite to that of the rotor. The air gains angular momentum which means an increase in its kinetic energy downstream of the turbine. This generation of rotational kinetic energy in the wake results in less energy extraction by the rotor than would be expected without wake rotation. In general the extra kinetic energy in the wind turbine wake will be higher if the generated torque is higher. Hence slow running wind turbines (with a low rotational speed and a high torque) experience more wake rotation losses than high speed wind machines with low torque.

The angular velocity imparted to the flow stream is defined as ω and is assumed to be small compared to the angular velocity, Ω . Across the disk, the angular velocity of the air relative to the blade increases from Ω to $\Omega + \omega$, while the axial component of the velocity remains constant assuming an ideal situation. The angular induction factor, a' , is defined as the relationship between the angular velocity imparted to the flow stream and the angular velocity of the rotor (Eq. 2.9).

$$a' = \frac{\omega}{2\Omega} \quad (2.9)$$

Assuming a control volume that moves with the angular velocity of the blade, the energy equation can be applied for the sections upstream and downstream of the blades to derive an expression for the pressure difference across the turbine [9]. The result (Eq. 2.10) can be inserted in Eq. 2.3 to show the theoretical thrust force at the disk (Eq. 2.11).

$$p_D^- - p_D^+ = \rho \left(\Omega + \frac{1}{2} \omega \right) \omega r^2 \quad (2.10)$$

$$dT = (p_D^- - p_D^+) dA \quad (2.11)$$

Equating the two thrust force expressions of linear momentum theory (Eq. 2.6) and angular momentum theory (Eq. 2.11) gives the expression Eq. 2.12, which is defined as the local and total tip speed ratio.

$$\frac{a(1-a)}{a'(1+a)} = \frac{\Omega^2 r^2}{V^2} = \lambda_r^2 \quad \lambda = \frac{\Omega R}{V} \quad (2.12)$$

Applying the conservation of angular momentum, an expression for the torque on the rotor can be derived. For this situation, the torque exerted by the rotor, dQ , must equal the change in angular momentum of the wake. Equation 2.13 shows this for an incremental annular area segment.

$$dQ = d \dot{m}(\omega r)(r) = (\rho V_D 2\pi r dr)(\omega r)(r) \quad (2.13)$$

Using Eq. 2.4 and Eq. 2.13 the expression can be reduced to Eq. 2.14.

$$dQ = 4a'(1-a) \frac{1}{2} \rho V \Omega r^2 2\pi r dr \quad (2.14)$$

The power generated at each segment equals the incremental torque of the rotor, multiplied by its angular velocity Eq. 2.15. The incremental and the total power coefficient can now be calculated Eq. 2.16 and Eq. 2.17.

$$dP = \Omega dQ \quad (2.15)$$

$$dC_p = \frac{dP}{dP_V} \quad (2.16)$$

$$C_p = \frac{8}{\lambda^2} \int_0^\lambda a'(1-a) \lambda_r^3 d\lambda_r \quad (2.17)$$

In order to integrate this expression, the variables a , a' , λ_r have to be related [10, 11]. Then a formula to express the maximum power coefficient can be derived [12].

The result of the analyses for maximum power coefficients including wake rotation is shown in Fig. 6. It also shows the Betz limit for an ideal turbine based on the previous linear momentum analysis. At higher tip speed ratios the maximum theoretical power coefficient increases.

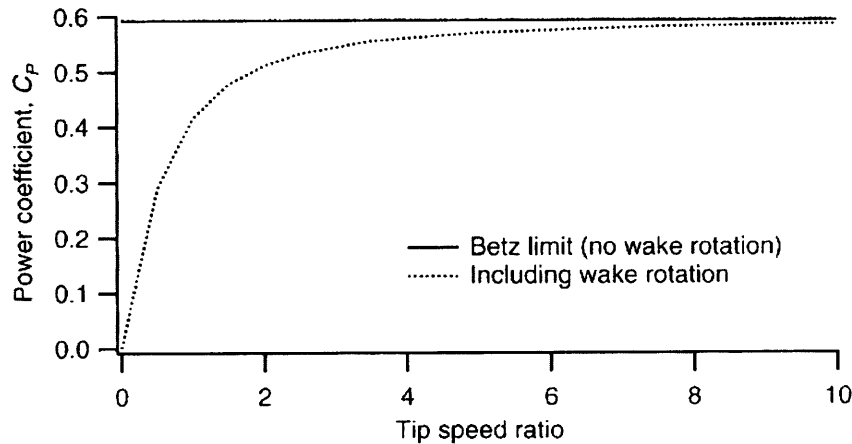


Fig. 6: Theoretical maximum power coefficients [12]

As an example, Fig. 7 shows results for an ideal wind turbine with wake rotation operating at a tip speed ratio of 7.5. The axial and the tangential induction factors vary in non-linear relationships over the blade span. The axial induction factor is (in this ideal example) very close to the optimal Betz value of $a = 0.33$.

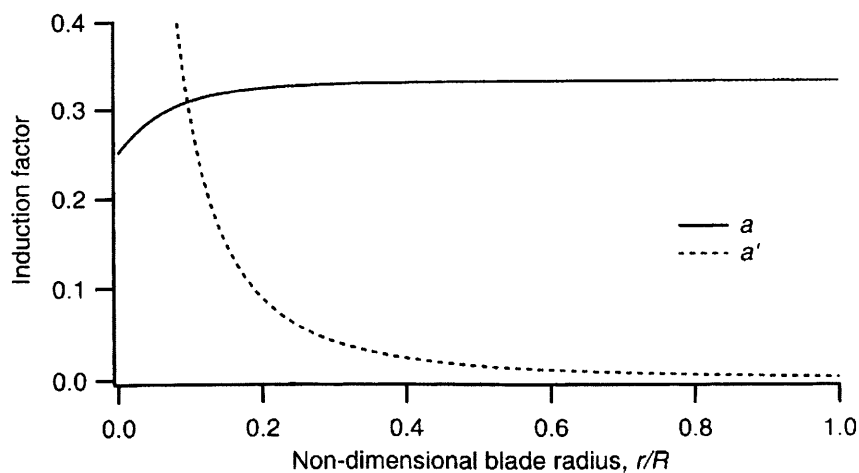


Fig. 7: Axial and tangential induction factors for an ideal HAWT, operating at $\lambda=7.5$ [12]

2.2. Wind turbine aerodynamics

The previous chapters showed the basic physics of theoretical wind power potential for wind turbines. The axial as well as the tangential momentum theories characterize the flow field of an ideal horizontal wind turbine. Both momentum theories in combination are still an oversimplification of real wind turbine operation. The laws of fluid dynamics, regarding vortices, drag and friction, have not yet been considered. In practice, a wind turbine's rotor makes use of airfoils to approach the theoretically achievable power extraction and for a detailed analysis, the respective laws of fluid mechanics need to be used.

2.2.1. Airfoils

An airfoil is a body with a shape similar to that shown in Fig. 8. The mean camber line is the locus of points halfway between the upper and lower surfaces of the airfoil. The chord length, c , is the distance from the leading to the trailing edge. The angle of attack, α , is defined as the angle between the relative wind direction and the chord line. Airfoils create a lifting force in a fluid flowing from a specific range of angles of attack. The flow velocity is higher over the convex surface resulting in lower average pressure on that side of the airfoil compared with high pressure on the bottom side of the airfoil. Friction also occurs between the fluid and the airfoil surface. The results are lift forces, drag forces and a pitching moment, this moment acts at a distance of $c/4$ from the leading edge (Fig. 9).

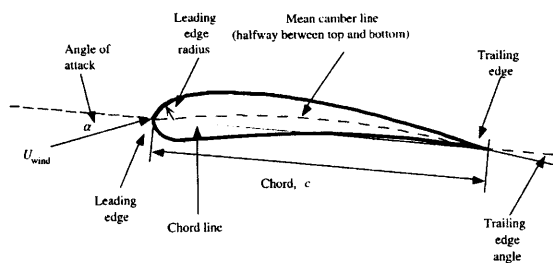


Fig. 8: Typical airfoil body shape [13]

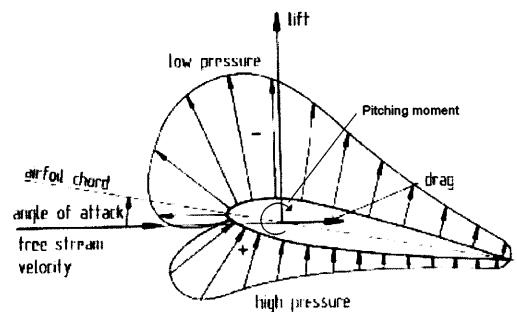


Fig. 9: Pressure distribution [13]

Flow characteristics of airfoils can be described by non-dimensional parameters. The most important parameter is the Reynolds number, Re , defined by Eq. 2.18, where, μ , is the fluid viscosity, ν , the kinematic viscosity. V and c describe the scale of the flow.

$$Re = \frac{Vc}{\nu} = \frac{\rho Vc}{\mu} = \frac{\text{Inertial force}}{\text{Viscous force}} \quad (2.18)$$

Other important coefficients are the two-dimensional lift coefficient, C_l (Eq. 2.19), the two-dimensional drag coefficient, C_d , (Eq. 2.20) and the pitching moment coefficient, C_m , (Eq. 2.21), where, L is the lift force, D is the drag force, and s is the airfoil span, here for a segment $s=1$.

$$C_l = \frac{L / s}{0.5\rho V^2 c} = \frac{\text{Lift force / airfoil span}}{\text{Dynamic force / airfoil span}} \quad (2.19)$$

$$C_d = \frac{D / s}{0.5\rho V^2 c} = \frac{\text{Drag force / airfoil span}}{\text{Dynamic force / airfoil span}} \quad (2.20)$$

$$C_m = \frac{M}{0.5\rho V^2 s c^2} = \frac{\text{Pitching moment}}{\text{Dynamic moment}} \quad (2.21)$$

Airfoil behavior can be categorized into three flow regimes, as shown in the example in Fig. 10: (1) attached airflow regime, at low angle of attack the flow is attached to the upper surface of the airfoil. The lift increases with the angle of attack and drag is relatively low. (2) High lift / stall development regime, the lift coefficient peaks until the angle of attack exceeds a certain critical value. At that value stall occurs and separation of the boundary layer on the upper surface takes place. This causes a wake to form above the airfoil, which reduces lift and increases drag. (3) Flat plate / fully stalled regime, at larger angles of attack (up to 90 degrees), the airfoil acts increasingly like a simple flat plate. At approximately 45 degrees the lift and drag coefficients are equal and at 90 degrees zero lift occurs. Literature provides deeper insights into airfoil theory [10, 14].

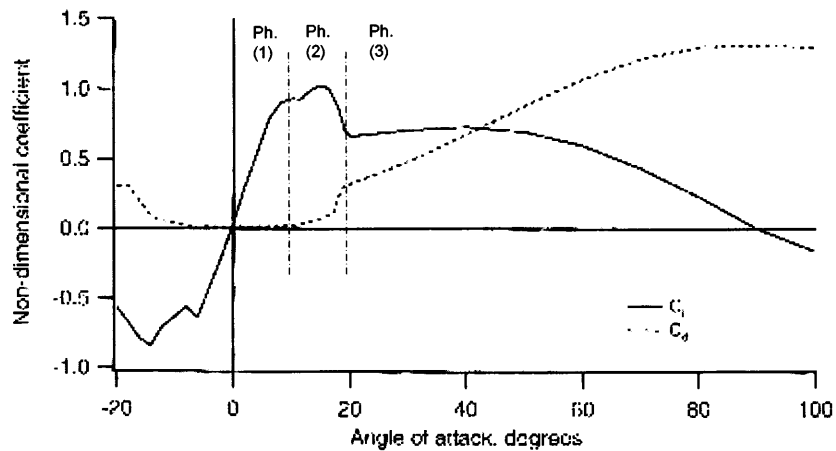


Fig. 10: Lift and drag coefficients for a S809 airfoil, at $Re=75,000,000$ [13]

Many types of airfoils exist, with various characteristics. The most well-known airfoil series (NACA) was developed by the National Advisory Committee for Aeronautics. The U.S. National Renewable Energy Laboratory has developed an airfoil family specifically optimized for the use in wind turbines, the S-xxx series.

2.2.2. Blade element theory

All modern wind turbines are designed to use the aerodynamic lift forces of their airfoil shaped rotor blades to create torque. For the purpose of analysis, the blade is divided into a number of independent segments (sections) along the blade length. At each segment a force balance is applied which takes into account 2D segment lift forces and drag forces, thrust forces and torque. Fig. 11 shows such a cross section.

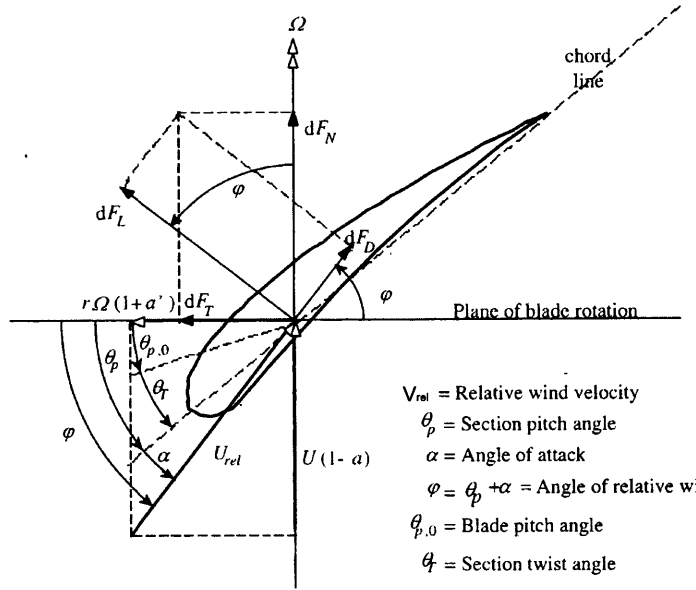


Fig. 11: Airfoil cross section of a wind turbine's rotor blade [13]

The attacking airflow velocity, V_{rel} , (Eq. 2.22) is the vector product of the perpendicular wind speed, V_D , and the relative rotational speed (which considers rotational speed and wake rotation). The relative rotational speed upstream of the disk is zero and immediately after the disk it can be derived from Eq. 2.9. For this case it is assumed that the rotational speed at the blade chord line is equal to $\Omega_r * a'$ (one half of the value immediately after the disc) [8].

$$V_{rel} = V \sqrt{(1-a)^2 + \left(\frac{r\Omega_r}{V} (1+a')\right)^2} = \frac{V(1-a)}{\sin \varphi} \quad (2.22)$$

In Fig. 11 the angle θ_p is the section pitch angle (the angle between the chord line and the plane of rotation), $\theta_{p,0}$ is the blade pitch angle, θ_T is the blade twist angle, α , is the angle of attack and φ , is the angle of relative wind. The vector sum of the incremental lift and drag forces on the rotor blade, dF_L and dF_D is equal to the vector sum of the resulting incremental forces normal to and tangential to the plane of rotation, dF_N and dF_T .

By setting up the equilibrium of forces around the blade section, the differential normal force, dF_N , (Eq. 2.23) and the differential torque, dQ , (Eq. 2.24) at a radial distance, r , can be derived.

$$dF_N = B \frac{1}{2} \rho V_{rel}^2 (C_l \cos \varphi + C_d \sin \varphi) c dr \quad (2.23)$$

$$dQ = B \frac{1}{2} \rho V_{rel}^2 (C_l \sin \varphi - C_d \cos \varphi) c r dr \quad (2.24)$$

From blade element theory, one obtains these two equations which are a function of the flow angles at the blade and airfoil of characteristics. High lift forces increase useful torque and drag forces decrease torque. Both forces contribute to normal forces and hence increase loading.

2.2.3. Blade element momentum theory

Blade element momentum theory (BEMT) combines the flow field characterization of axial and tangential momentum theories with the aerodynamic properties of the turbine's rotor blades in order to calculate resulting forces and hence the performance of the turbine. The momentum theories refer to a control volume of the forces at the blade based on the conservation of linear and angular momentum. They give the theoretical limits of wind power potential. The blade element momentum theory refers to an analysis of forces at a section of the blade, as a function of blade geometry.

A set of non-linear equations, which have been derived in previous sections, govern the blade element momentum theory (Eq. 2.6, Eq. 2.14, Eq. 2.23, Eq. 2.24). Equating the formulas yields no closed form analytical solution, since lift and drag coefficients are empirical or based on computational results. Instead, the formulas have to be solved by iteration for each blade section. The resulting values of section thrust and torque can be integrated to predict the overall performance of the wind turbine.

2.2.4. Iterative solution method of the BEMT

The solution of the BEMT has to be found using an iterative numerical approach. The fundamental procedure will be explained subsequently. In the performance simulation code for wind turbines "WT_perf" (developed by the NREL) this approach is the foundation to calculate

wind turbine characteristics. The code has also been extended to consider various other aerodynamic effects which will be discussed later.

The calculation of the following characteristics has to be performed incrementally for each section of the blade.

In order to reduce complexity significantly, the accepted practice in the calculation of induction factors a and a' is to set C_d to zero [15]. For airfoils with low drag coefficients, this simplification introduces negligible errors. With C_d equal to zero, equating the formulas Eq. 2.6, Eq. 2.14, Eq. 2.23, Eq. 2.24 and using some algebraic manipulations yield Eq. 2.25 and Eq. 2.26. The local blade solidity, σ' , is defined as Eq. 2.27.

$$a = \frac{\sigma' C_l \cos \varphi}{1 + 4 \sin^2 \varphi} \quad (2.25)$$

$$a' = \frac{1}{\frac{4 \cos \varphi}{\sigma' C_l} - 1} \quad (2.26)$$

$$\sigma' = \frac{Bc}{2\pi r} \quad (2.27)$$

The first step in the iteration process is to guess values of a and a' . Different practices for first estimates exist and the WT_perf code starts assuming that no induction effect exists. In the second step the angle of relative air flow attack is calculated (Eq. 2.28) using geometries from Fig. 11.

$$\alpha = \varphi - \theta_p = \tan^{-1} \left(\frac{V(1-a)}{\Omega r(1+a')} \right) - \theta_p \quad (2.28)$$

Knowing the angle of attack and being able to calculate the Reynolds number using Eq. 2.18 and Eq. 2.22, the lift and drag coefficients have to be looked up in empirical data tables or calculated using CFD- or panel-codes (e.g. XFOIL). Finally new induction coefficients can be calculated with the help of Eq. 2.25 and Eq. 2.26. Using the new values for the induction, the process shall

be repeated until the induction factors change less than a certain amount from one iteration to the next. In practice the demonstrated solution method is extended using Prandtl's tip-loss algorithm, hence it becomes much more complex [7].

3. Rotor design and simulation

3.1. Rotor design procedure based on BEMT

The design of the perfect rotor blade is a very complex process, since an infinite number of design possibilities exist. The turbine has to operate as effectively as possible under a range of conditions but also has to provide durability and allow ease of fabrication. Design parameters are rotor diameter, number of blades, airfoil types, chord length distribution, twist distribution, material and blade construction. Parameters for operation include the tip speed ratio and the pitch angle of the blades.

In general, the design and construction process in the wind turbine industry as well as in the aviation industry is performed in an iterative fashion [53]. However, work has been performed to approach the blade design problem in a more direct manner. This alternative allows the designer to input desired rotor performance characteristics and blade aerodynamic characteristics and use the BEMT code to determine the corresponding twist and cord distribution. These semi-reverse design processes are steps towards a fully automated design process.

A generalized manual design procedure can be performed by following the suggested steps.

(1) Determination of basic rotor parameters, knowing the expected power output, P , at a particular wind speed, the radius of the rotor can be estimated from Eq. 2.29. The formula includes the effect of a probable C_p and efficiencies of other components, η , (e.g. gearbox, generator). A number of rotor blades, B , and a corresponding tip speed ratio, λ , have to be chosen. The higher speed machines use less material and have smaller gearboxes, but require more sophisticated airfoils. Table 6 gives a brief overview of the relationship between blade number and tip speed ratio.

$$P = C_p \eta \frac{1}{2} \rho \pi R^2 V^3 \quad (2.29)$$

Table 1: Suggested blade number, B, for a given tip speed ratio, λ

λ	B
1	8-24
2	6-12
3	3-6
4	3-4
>4	1-3

(2) Determination of the blade shape, airfoil shapes for the rotor have to be chosen or created. The selection of the initial shape is usually based on experience. The airfoil shape's aerodynamic characteristics (C_l vs. α and C_d vs. α for a range of Re numbers) have to be obtained and the initial design conditions should be selected such that C_d / C_l is minimized for each blade section. This does not represent optimal design but is a good value to start with. The rotor blade's optimal chord length and pre-twist distribution are to be calculated using Eq. 2.30 and Eq. 2.31. The optimization, derived from the blade element momentum theory [7], includes wake rotation but ignores tip-losses and drag which are negligible, see[15].

$$c_{(opt)}(r) = \frac{16R^2\pi}{9BC_l\lambda^2r} \quad (2.30)$$

$$\varphi(r) = \arctan\left(\frac{2R}{3r\lambda\left(1 + \frac{2R^2}{3\lambda^2r^2}\right)}\right) \quad (2.31)$$

(3) Determination of induction factors: Induction factors a and a' should be determined using an iteration method similar to the method described in the previous section, but it should be extended by Prandtl's tip-loss algorithm.

(4) Determination of the power coefficient: Having solved the equations for the performance for each blade section, the power coefficient is determined by solving the integral in Eq. 2.32 which is derived from the BEMT, incorporating the tip-loss factor, F.

$$C_p = \frac{8}{\lambda^2} \int_{\lambda_h}^{\lambda} F \sin^2 \varphi (\cos \varphi - \lambda_r \sin \varphi) (\sin \varphi + \lambda_r \cos \varphi) \left[1 - \left(\frac{C_d}{C_l} \cot \varphi\right)\right] \lambda_r^2 d\lambda_r \quad (2.32)$$

(5) Modify the design and repeat Steps 1 to 4 in order to find the best design for the rotor.

The above rotor design procedure based on the blade element momentum theory is the basis for most computational simulation codes which are based on engineering models. In practice the procedures are more complex and have been continually optimized over the last 30 years.

3.2. Computational aerodynamic simulation of wind turbines

There are a number of comprehensive models that have been developed for the analysis of wind turbine aerodynamics. Those can be subdivided into engineering models and computational fluid dynamics methods. Most engineering models are based on the blade element momentum theory (BEMT). Wake models which predict the wind speed decrease behind the turbine also belong to the category of engineering models.

Computational fluid dynamic methods numerically solve the Euler or Navier-Stokes equations from first principles.

Blade Element Momentum Theory. The majority of computer codes for wind turbine analysis are based on the blade element momentum theory. A major advantage of BEMT based codes is the flexibility to include a wide range of validated subcomponent models representing various physical effects that are difficult to model from first principles. This approach also allows the subcomponent models to be validated against idealized laboratory experiments. Subcomponent models include inflow models, vortex models or Prandtl's tip- and hub-loss algorithms. Inflow- and vortex models represent the non-uniform induced velocity associated with the vertical wake trailed from a turbine. They can eliminate limitations associated with a range of analyzable operating conditions (e.g. tilt, yaw, etc.). Losses due to vortices at the blade tip and hub are usually addressed by implementing Prandtl's tip- and hub-loss algorithms. BEMT's can also be

combined with structural dynamic models to produce powerful aeroelastic tools for the detailed structural design of wind turbines.

Airfoil characteristics for the full range of probable operating cases need to be obtained and integrated in the BEMT analysis. 2D CFD codes or panel codes (e.g. xfoil, profil, ellipsys 2D, ADINA) can be used to provide the necessary dataset. The original BEMT code is the PROP code, developed in 1974 at the Ohio State University. The most updated code from NREL, WT_perf is still based on PROP but has been improved significantly. The code of the Risø National Laboratory is an aero elastic code, called HAWC.

Computational Fluid Dynamic (CFD). Based on numerical solutions to the Euler and Navier-Stokes equations CFD has the potential to provide a consistent and physically realistic simulation of the turbine flow field. The high computational costs and numerous numerical issues associated with CFD methods means that they have not yet seen significant use in wind turbine applications. In particular, problems involving flow separation, such as dynamic stall have proved challenging for Navier-Stokes based methods. Also the prediction of the three-dimensional vertical wake behind a turbine causes as yet unsolved challenges. While researchers have begun to take up the challenge of modeling wind turbine problems using CFD, the accuracy of these methods has not yet been validated sufficiently [53]. With faster computers and improved algorithms, CFD will ultimately prevail over engineering models for the design of better and more efficient wind turbines. The Risø National Laboratory has developed the well-known EllipSys3D code for wind turbine simulations.

3.3. Comparison of simulation programs

The most effective way to compare and evaluate simulation tools is to benchmark against experimental data and other tools. One extensive benchmark has been performed so far under the organization of the U.S. National Renewable Energies Laboratory [16]. It was a significant collaborative effort on the part of the international wind turbine research community and has shown that wind turbine physics is much more complex than was assumed by state of the art physical and mathematical models. The participants of the benchmark study represent an international assortment of industry, academic and government organizations specializing in wind turbine performance and load modeling. The list of the 17 participating organizations comparing 21 simulation codes can be seen in Table A1. However the results were not associated with specific organisations.

The initial starting point of the benchmark was the design of the NREL Ph. VI wind turbine and extensive wind tunnel experiments in the NREL/NASA-Ames wind tunnel, the largest of its kind. Steady state wind conditions can only be simulated in wind turbine experiments. The test data were not revealed prior to the blind comparison.

The simulation results were grouped into four basic modeling-tool categories to facilitate comparison: (1) Performance codes, (2) aeroelastic codes, (3) wake codes and (4) CFD codes. The assignment is somewhat arbitrary and subjective since some models use combinations of methodologies.

A total of 20 different operating cases (e.g. wind speeds, yaw angles, etc.) were simulated by each participant. The main benchmark characteristics are (1) normal force coefficient, (2) tangent force coefficient, (3) pitch moment coefficient, (4) flap bending moment and (5) local dynamic pressure. All benchmarks (considered at three radial blade locations) can be looked up in [74]. The key data can also be used to calculate the power coefficient.

The results of the comparison show that there is neither a clear winner nor a clear loser. All code predictions were equally inconsistent in that they tended to sometimes predict wind tunnel results under certain conditions, but then failed under other conditions. One code was outstanding in predicting turbine performance and loads under zero yaw conditions. This was a 3D incompressible Navier Stokes CFD model. It consistently delivered the best results in predicting aerodynamic forces distributed along the blade span, but was only able to simulate the simplest

case and it took days of computer time to run one case. This code gave poor results when simulating airfoils other than the S809 and is therefore not yet sufficient. However, overall CFD codes have the highest potential but are not yet practical modeling tools for wind turbine tradeoff studies. Performance or aeroelastic codes based on BEMT, and incorporating inflow- and vortex models, are currently the most practical codes and are widely used in research and industry.

4. Analysis of wind turbine optimization possibilities

The results from wind turbine axial momentum theory (Ch. 2) can be summarized to give four key insights:

- The power of wind flow and hence the power convertible by a turbine increases with rising wind speed to the power of three (Eq. 2.1).
- The power of a turbine increases linear by the area size of the actuator disc and, therefore, it rises to the power of two with its diameter (Eq. 2.1).
- Alfred Betz has proven that the theoretically maximum possible power coefficient of any wind energy conversion system is limited to 59% (Eq. 2.8).
- At the highest possible efficiency rate (0.59) the wind velocity at the plane of rotation is equal to $2/3$ of the free-stream velocity (Eq. 2.4).

4.1. Loss factors in steady state operation

The theoretical efficiency of the axial momentum theory can never be achieved in practice as the construction of an ideal rotor is not feasible. A variety of losses occur in the operation of a wind turbine. These are subject to the laws of fluid mechanics and have been discussed in Ch. 2. These aerodynamic losses include:

- Profile drag:
The aerodynamic drag of the airfoil depends on the Re-number, the angle of airflow attack, the profile geometry and the surface structure. At low Re-numbers ($Re < 5 \times 10^5$) friction predominates, at higher Re-numbers pressure drag predominates.

- Wake rotation:

The consequence of the reaction torque of the moving rotor blade is a wake rotation behind the turbine over the whole span of the blade. The tangential induction factor a' characterizes this wake. The ideal distribution of a' is shown in Fig. 15. With rising rotational speed of the rotor the tangential wake decreases.

- Hub- and tip-losses:

Having a finite rotor blade or airplane wing, pressure compensation occurs on the edges (hub, tip) which on one hand results in vortices and reduces the lift forces close to the edges. Prandtl has analyzed this phenomenon [7].

In order to approach the Betz limit, the turbine design has to consider the listed aerodynamic restriction but also has to comply with the axial momentum theory. The optimal rotor design is always restricted to the design-tip speed ratio. Fig. 7 shows the optimal induction factors for an ideal wind turbine at $\lambda = 7.5$. A wind turbine operated at other than the design-tip speed ratio will result in a deviation of the optimal wind speed reduction (a), will lead to a non-optimal wake rotation (a') and will operate under less ideal aerodynamics.

4.2. Passively adaptive wind turbine blades

The investigation of loss factors shows that adaptation of the blade shape has the ability to optimize the efficiency for operating conditions other than the design-tip speed ratio. For larger wind turbines pitch control mechanisms are installed in order to adapt the angles of airflow attack. For small or medium size wind turbines such systems are often not profitable.

Global pitch control systems can only linearly adapt to the optimal angle of attack. However, in practice the optimal angle of attack varies non-linearly over the blade span. The reasons for this behavior include:

(1) chord length distribution: Having a linear chord distribution, the Re-numbers vary nonlinearly when wind velocity changes. Hence changes of local angles of attack are distributed non-linearly. For this reason a formula for the optimal chord length (Eq. 2.33) has been developed [7].

$$c_{opt}(r) = \frac{16\pi R^2}{Z9C_L\lambda_R^2 r} \quad (2.33)$$

Using Eq. 2.33 in the design process would lead to linear changes of the AoA due to chord distribution, but at the inner third of the blade radius, the optimal chord lengths become too large for implementation. As a result even for optimized blades a non-ideal part will always remain.

(2) Non-linear changes of airfoil characteristics: Airfoil characteristics deviate non-linearly with changing fluid velocities, which as a result cause non-linear changes of optimal angles of attack.

(3) Non-linear distribution of axial and tangential induction factors.

(4) Radial interactions between flows through continuous annuli of the rotor blade (3D effect).

(5) Non-uniform distributed inflow of the wind speed, due to natural irregularities in the wind field.

Locally adaptive rotor blades would have the possibility to change blade characteristics for each blade segment individually. Advantages of adaptive rotor blades can be of different types according to the turbine's operating and design characteristics. The desired reaction of adaptive blades also depends on these characteristics. Table 7 shows an overview on improvement possibilities for wind turbines. In general, passively adaptive rotor blades (PARB) can be a cost effective solution to enhance small or medium wind turbines, when gearboxes and pitch controls are not profitable. The asymmetric composition of advanced composite materials will most likely provide a passively adaptive solution at minimal increasing production costs. For this purpose two options are possible:

Option (1), Efficiency improvement. A report on aero-elastic tailoring concludes that bending-twist coupling towards feather gives the potential for a few percentages of energy yield improvement for constant-speed pitch-controlled turbines, and improves starting torque by 10% [17]. Another study analyzing this topic found that large angles of pitch (up to 30° - 40° at the tip) are required to achieve the improvement [18].

Option (2), twist rotor blades towards stall and reduce blade loading. A report of the SANDIA laboratory has examined this case [19]. The blade was assumed to twist to stall, reducing maximum power. The rotor diameter was then increased to bring rotor power back up to the initial level. For this case a maximum twist of one degree lead to an energy increase of 5%; a maximum twist of two degrees lead to an energy increase of 10%. Other simulations estimate

maximum annual energy gains of around 25% for fixed pitch turbines [17]. The downside of this configuration is the negative effect on stability.

For large turbines adaptive blades have the possibility to better react on gusts or irregular flow fields. Especially since global pitch mechanisms are quite slow for large sized turbines.

It has been found that adaptive blades also have the possibility to reduce vibration and fatigue loads by up to 10% [20]. The largest European research project in wind energy “Up-wind” is currently researching non-linear adaptive rotor blades for large turbines.

Table 7: Typical HAWT’s and their optimization potential using PARB’s

	Size of Wind Turbine			
	Small	Medium (1)	Medium (2)	Large
Typical characteristics				
Variable speed control:	no	no	yes	yes
Variable pitch control:	no	yes	no	yes
Stall control:	yes	yes	yes	yes
Optimization potential using adaptive rotor blades				
Efficiency enhancement:	high	medium	low	low
Load reduction and permitting larger rotors:	high	low	medium	high
Reaction on gusts and irregular wind flow:	low	medium	medium	high

In conclusion, passively adaptive rotor blades can improve the efficiency by twisting towards feather or decrease loads by twisting to stall. In the design of wind turbines the following considerations should be analyzed:

- Small-size wind turbine: Does the efficiency increase or load reduction of additional PARB’s compensate for higher investment costs?
- Medium-size wind turbine: Are PARB’s a less expensive solution than classical pitch control systems?
- Large-size wind turbine: Have PARB’s the ability to further improve pitch control systems and are the higher costs economically?

PARB solutions are complex to design and they have not yet found applications in commercial wind turbines. It is most likely that further research on passively adaptive rotor blades will enable turbine improvements in the future.

5. A numerical procedure for the design of passively adaptive turbine blades

The preceding chapter has shown that the possibilities to enhance wind turbines by using adaptive rotor blades. Using active blade adaptivity realized by flaps or piezoelectric effects, will probably not be a successful option. Passive adaptivity on the other hand, given by asymmetric deformational change of non-isotropic materials, might be a possibility to improve wind turbine blades at minimal increasing costs.

In order to design a power enhancing PARB, a numerical procedure (Fig. 12) has been developed. The basic concept is that the blade should perform deformations proportional to rising wind speeds in order to approach the specific optimal shape and hence increase its power conversion efficiency. The deformation should be induced by material properties as a result of increasing bending forces.

The starting point of the overall analysis and design process must be a given turbine design including its operating conditions. The wind speed of operation has to be split into a defined finite number of speeds for the analysis. For each of these wind speed steps, the rotational speed and the blade pitch angle have to be given. The original design characteristics of the rotor (necessary for the analysis) are: the radius, the number of blades, the airfoil type and the pre-twist and chord distribution over the blade span. For the analysis, the rotor blade is divided into a finite number of segments. The procedure for passively adaptive blade design (Fig. 12) consists of two major components: (1) the aerodynamic simulation and (2) the structural simulation.

Procedure for passively adaptive blade design

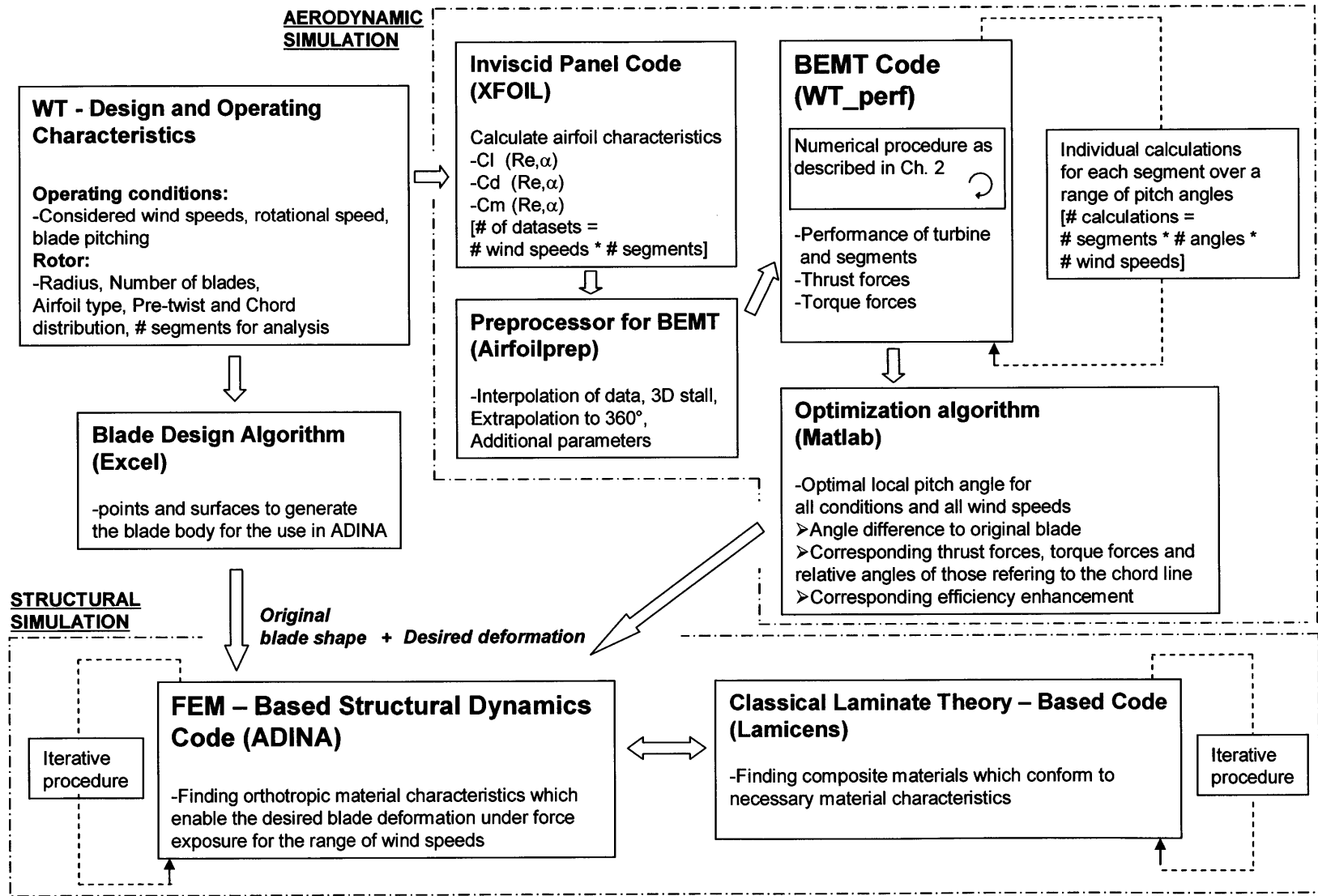


Fig. 12: A procedure for the design of passively adaptive rotor blades for wind turbines

5.1. Aerodynamic simulation

The developed aerodynamic simulation procedure aims to find the optimal angle of attack (AoA) for each blade section over the range of wind speeds. The optimal AoA is the angle of airflow attack on an airfoil segment that generates the largest possible power output.

At first, the aerodynamic characteristics (Ch. 2.2.1) of the airfoil shaped rotor blade have to be determined. In order to approach the coefficient values distributed over the blade, a two-dimensional panel method is applied for each blade section by using the code XFOIL, developed by Prof. M. Drela at the Massachusetts Institute of Technology. The calculations depend on the Reynolds number (Eq. 2.18) and hence each blade section has to be calculated for the range of wind speed steps individually.

The results (similar to Fig. 10) have to be adapted to the required form of the used BEMT code. For this procedure, the preprocessor AIRFOILPREP, developed by the U.S. National Renewable Energy Laboratory, is applied. The XFOIL data are interpolated to integral numbers of the AoA, α . For a rotating airfoil, such as in a turbine, the actual airfoil properties differ from the calculated values. The AoA at which stall occurs is greater for a rotating blade than for the same blade tested statically [7]. This phenomenon is called delayed stall and was first noticed by Himmelskamp (1945). The 3D stall delay adaptation in AIRFOILPREP uses the stall delay model presented in [21].

Panel codes typically do not calculate airfoil data over the entire range of 360° . Since the entire range is necessary for wind turbines, data extrapolation has to be performed. The aerodynamic characteristics of an airfoil generally become independent of its shape for the Phase 3 (presented in Ch. 2.2.1). Airfoil data for this range are calculated using flat plate theory.

Provided with these necessary datasets, the performances and forces of each segment of the wind turbine can be calculated by using the blade element momentum code WT_perf, developed at the National Renewable Energy Laboratory (NREL). A large number of calculations have to be performed in order to analyze the range of AoA's for each section and all wind speeds.

Having computed a performance database, an optimization algorithm is applied to find the optimal local pitch angles for each segment varying over wind speed. Integrating over the corresponding partial performances, gives the new power curve of an adaptive rotor blade. Resulting thrust forces, torque forces and the angle differences to the original blade for all segments are being calculated as well.

The optimal shape deformation of the blade over wind speed, including its characteristics, has been determined.

5.2. Structural response simulation

The optimal blade deformation has been determined in the aerodynamic simulation process. In order to achieve the desired deformations due to the material response generated by the loads, structural dynamic simulations have to be performed. The FEM program ADINA, developed by ADINA Inc., was used for the analysis

At first, the rotor blade characteristics, such as radius, airfoil type, pre-twist and chord distribution, are used to generate a large number of points which describe the outer shell of the blade's body. The algorithm in Excel also creates surface datasets which are converted into an ADINA input file.

Having implemented the original blade shape in ADINA and knowing the desired incremental deformations as well as the incremental force changes, an iterative procedure can be executed to find suitable materials which enable the desired deformation. Starting points for the iterative procedure are logical material hypotheses discussed in Ch. 5.4. The simulation of different material behavior in a structural dynamics code is accompanied by a classical laminate theory code, LAMICENS, developed by Prof. H. Funke at the University of Dortmund, which is used to iteratively find the best possible material to suit the desired material characteristics.

5.3. Structural and material design

Composite rotor blades have been widely used as an important part of wind power generation systems because strength, stiffness, durability and vibration of composite materials are all excellent [22]. The strongest and stiffest construction materials which are available are carbon-fibres in an epoxy resin matrix. Due to lower costs, most blades are built out of lightweight glass-reinforced plastic (GRP) with an epoxy or polyester resin matrix.

These composite materials are usually designed to be isotropic, which means that properties are independent of direction. In order to achieve properties which are dependent on direction, anisotropic materials are necessary. A special case of anisotropy is called orthotropy and these materials have different properties defined in two directions. The general stress-strain relation is given by Hooke's law, Eq. 2.34, where σ is the stress, C is the stiffness matrix and ε is the strain. For further details, see [23].

$$\varepsilon = \sigma * C^{-1} \quad (2.34)$$

For elastic orthotropic materials, the general form in Eq. 2.34 reduces to Eq. 2.35, where e is the normal strain, γ is the shear strain, E is the Young's modulus, ν is the Poisson ratio and G is the shear modulus [24].

$$\begin{bmatrix} e_a \\ e_b \\ e_c \\ \gamma_{ab} \\ \gamma_{ac} \\ \gamma_{bc} \end{bmatrix} = \begin{bmatrix} 1/E_a & -\nu_{ab}/E_b & -\nu_{ac}/E_c & 0 & 0 & 0 \\ -\nu_{ba}/E_a & 1/E_b & -\nu_{bc}/E_c & 0 & 0 & 0 \\ -\nu_{ca}/E_a & -\nu_{cb}/E_b & 1/E_c & 0 & 0 & 0 \\ 0 & 0 & 0 & 1/G_{ab} & 0 & 0 \\ 0 & 0 & 0 & 0 & 1/G_{ac} & 0 \\ 0 & 0 & 0 & 0 & 0 & 1/G_{bc} \end{bmatrix} \begin{bmatrix} \sigma_a \\ \sigma_b \\ \sigma_c = 0 \\ \sigma_{ab} \\ \sigma_{ac} \\ \sigma_{bc} \end{bmatrix} \quad (2.35)$$

Equation 2.35 shows how the material deformation, expressed by normal and shear strains, depends on the stresses and the material properties in different directions. Asymmetric lay-ups of composite materials will provide these differences in characteristics. In the fiber direction, composite materials usually have high Young's modulus and are very stiff, but orthogonal to fiber directions they are more flexible.

The hypothesis in this thesis is that orthotropic material characteristics will provide a bend-twist action when having the axis of bending at an angle not equal to 90° or its multiples. The strongest effect is expected for angles of 45° or its multiples.

A simple orthotropic material simulation in ADINA illustrates this presumption. The simulated material is stiff in the direction of axis “a” and more flexible in the direction of axis “b”. By applying an equally distributed pressure on the beam in Fig. 13, it is shown that the beam bends stronger in the direction of less stiffer material properties. This in turn creates a bend-twist situation.

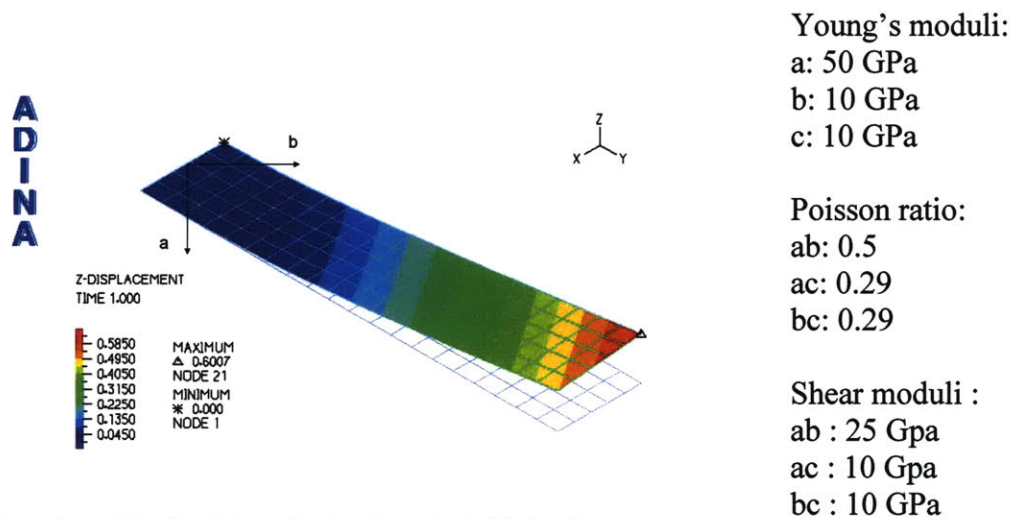


Fig. 13: Experiment to simulate orthotropic material behavior

These results, that show how orthotropic composite materials behave, will be used as the starting point in the structural dynamic simulation in the procedure for the design of passively adaptive rotor blades.

The simulation code LAMICENS used in the developed procedure is based on classical laminate theory and only simulates materials in the two-dimensional mode. A sensitivity analysis of the bend-twist experiment, shown in Fig. 13 has been performed using ADINA and the results are given in Table 8.

Table 8: Sensitivity analysis of the bend-twist experiment

Sample configuration	Z-Displacement		Twist (alpha)	Deviation from Original	Simulation dimension
	Node 126	Node 21			
Original	0.492	0.601	3.11	/	/
Young's modulus "a" + 10%	0.489	0.600	3.18	2.5%	2D
Young's modulus "a" + 100%	not possible	not possible	/	/	2D
Young's modulus "b" + 10%	0.458	0.555	2.77	-10.9%	2D
Young's modulus "b" + 100%	0.297	0.339	1.20	-61.3%	2D
Young's modulus "c" + 10%	0.492	0.601	3.11	0.0%	3D
Young's modulus "c" + 100%	0.492	0.601	3.11	0.0%	3D
Poisson ratio "ab" +10%	0.483	0.591	3.10	-0.2%	2D
Poisson ratio "ab" +100%	0.394	0.500	3.04	-2.1%	2D
Poisson ratio "ac" +10%	0.492	0.601	3.11	0.0%	3D
Poisson ratio "ac" +100%	0.492	0.601	3.11	0.0%	3D
Poisson ratio "bc" +10%	0.492	0.601	3.11	0.0%	3D
Poisson ratio "bc" +100%	0.492	0.601	3.11	0.0%	3D
Shear modulus "ab" +10%	0.485	0.593	3.08	-0.7%	2D
Shear modulus "ab" +100%	0.448	0.550	2.94	-5.4%	2D
Shear modulus "ac" +10%	0.492	0.600	3.11	0.0%	3D
Shear modulus "ac" +100%	0.488	0.597	3.10	0.0%	3D
Shear modulus "bc" +10%	0.491	0.600	3.10	-0.1%	3D
Shear modulus "bc" +100%	0.486	0.594	3.08	-0.9%	3D

The analysis shows that the Young's modulus in the "a" and "b" direction have the highest impact on the bend-twist functionality of the material. The Poisson ratio and the Shear modulus also have a small impact, but in both cases only in the "ab" effect. All material characteristics which are effective in the "c" direction, and hence can not be simulated by the code LAMICENS, have no or only a minor impact (less than 1%) on the bend-twist characteristics of the material. The material investigation has shown that orthotropic materials will provide a bend-twist effect and it proves by experiment that the code LAMICENS is sufficient for the simulation of suitable composite materials.

5.4. FSI coupling

The PARB design procedure (Fig. 12) includes an optimization algorithm to define the ideal shape deformation and calculates corresponding aerodynamic forces. However, when designing a real PARB, shape deformations will result in changes in aerodynamic loading. These dependencies actually make the system a coupled problem. In order to consider structural and aerodynamic coupling effects in the design procedure, the procedure has been extended by a FSI correction loop. Fig. 14 shows this extension of the procedure. An important requirement before the implementation is to find the stiffness properties of the real structure under the corresponding loading.

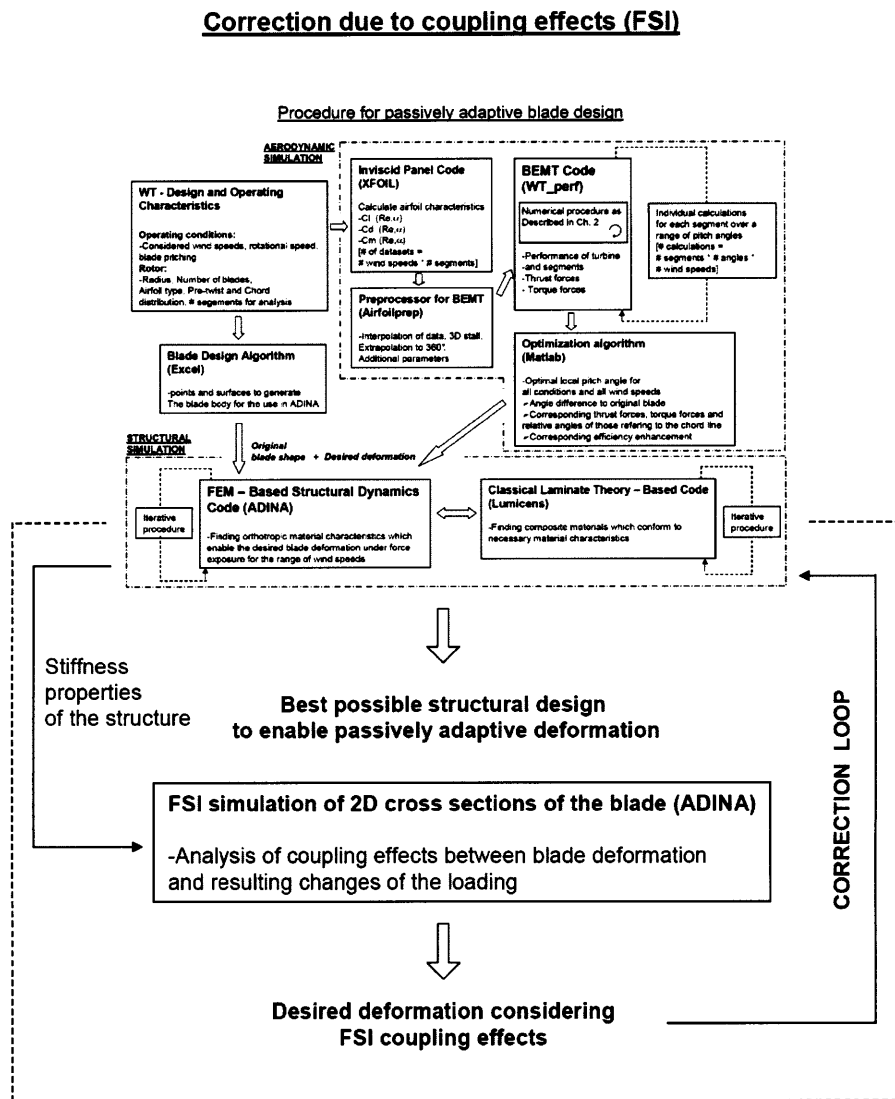


Fig. 14: Correction of coupling effects (FSI)

6. Airfoil analysis

6.1. The S809 airfoil

The S809 airfoil is a 21% thick wind turbine airfoil that has been designed at NREL by Somers [25]. The two primary design criteria were restrained maximum lift, insensitive to surface roughness, and low profile drag. The blade shape's characteristics suit well for the use in wind turbines. The foil section coordinates are shown in table 8. Fig. 15 graphically shows the shape of the airfoil.

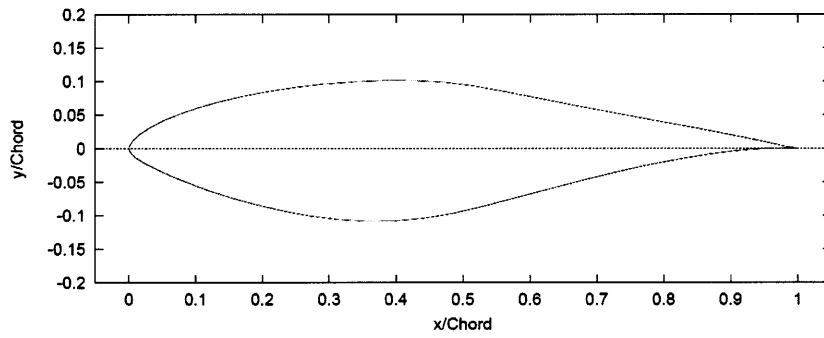


Fig. 15: Profile of the airfoil S809

Table 8: Airfoil geometry coordinates

<u>x</u>	<u>y (upper surface)</u>	<u>x</u>	<u>y (lower surface)</u>
1.00000	0.00000	0.00000	0.00000
0.99623	0.00054	0.00140	-0.00498
0.98528	0.00245	0.00933	-0.01272
0.96799	0.00600	0.02321	-0.02162
0.94523	0.01101	0.04223	-0.03144
0.91763	0.01694	0.06579	-0.04199
0.88537	0.02335	0.09325	-0.05301
0.84854	0.03017	0.12397	-0.06408
0.80756	0.03761	0.15752	-0.07467
0.76314	0.04578	0.19362	-0.08447
0.71606	0.05462	0.23175	-0.09326
0.66718	0.06403	0.27129	-0.10060
0.61747	0.07379	0.31188	-0.10589
0.56801	0.08356	0.35328	-0.10866
0.52005	0.09237	0.39541	-0.10842
0.47384	0.09843	0.43832	-0.10484
0.42809	0.10101	0.48234	-0.09756
0.38223	0.10109	0.52837	-0.08697
0.33689	0.09933	0.57663	-0.07442
0.29259	0.09594	0.62649	-0.06112
0.24987	0.09113	0.67710	-0.04792
0.20920	0.08505	0.72752	-0.03558
0.17103	0.07786	0.77668	-0.02466
0.13580	0.06972	0.82348	-0.01559
0.10390	0.06082	0.86677	-0.00859
0.07568	0.05132	0.90545	-0.00370
0.05147	0.04143	0.93852	-0.00075
0.03158	0.03136	0.96509	0.00054
0.01626	0.02133	0.98446	0.00065
0.00575	0.01166	0.99612	0.00024
0.00037	0.00275	1.00000	0.00000

6.2. CFD simulations

Airfoils can be simulated by using computational fluid dynamic codes. For this analysis ADINA has been used to compute the pressure distribution on 2D airfoil sections. The results have been compared to experimental data [25] or to panel code simulations from XFOIL. It is important to validate the fluid mechanical model in order to trust the subsequent FSI analysis. Furthermore, extensive airfoil characteristics are necessary input data in the BEMT wind turbine analysis.

6.2.1. CFD Model, boundary conditions and loading

The used model is a 2D domain of air. The S809 airfoil is surrounded by a circular flow field of a radius 8 times the foil's chord length. The foil is considered as rigid and its surface is considered as a wall to which the free slip condition has been applied. The flow field has been meshed with 43,000 elements. These elements are small near the airfoil and become larger towards the outer part of the flow field. It has been shown that the mesh has to be exceptionally fine at the leading edge in order to get good results. Fig. 16 schematically shows the construction of the model.

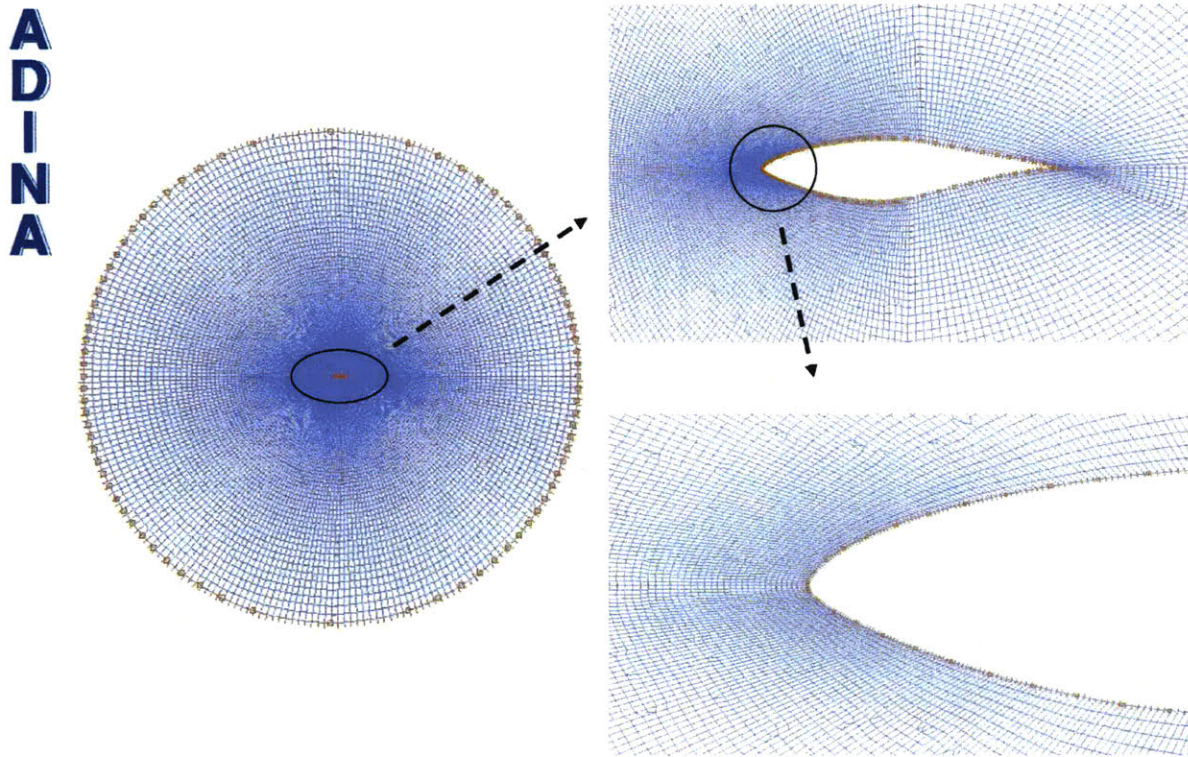


Fig. 16: S809 CFD model

For the subsequent FSI analysis the foil operates in the conditions of a wind turbine at 9m/s wind speed, a rotational speed of 72 rpm, a rotor radius of 4.125m, an air density of 1.204 Kg/m³ and a dynamic viscosity of 1.8 x 10⁻⁵ [Kg/ m s]. Using Eq. 2.18, these conditions result in a Reynolds number of 908,579.

The experimental data and the simulation data in reference [26] are performed at a Reynolds number of 1 x 10⁶, which is very close to our practical data. Hence the CFD validation against these data will show that the CFD simulations work properly and can be used in the wind turbine conditions.

The CFD model has been solved for several cases of different angles of attack, 0°, 6°, 10°, 12°, 14°. The subsequent FSI analysis will run at 12° (+/- 2°), which is in the range of the validation experiments.

6.2.2. The CFD results

Solving the established CFD model for the 5 angles of attack, results in the following solutions. Figs. 17 to 21 show the corresponding pressure fields.

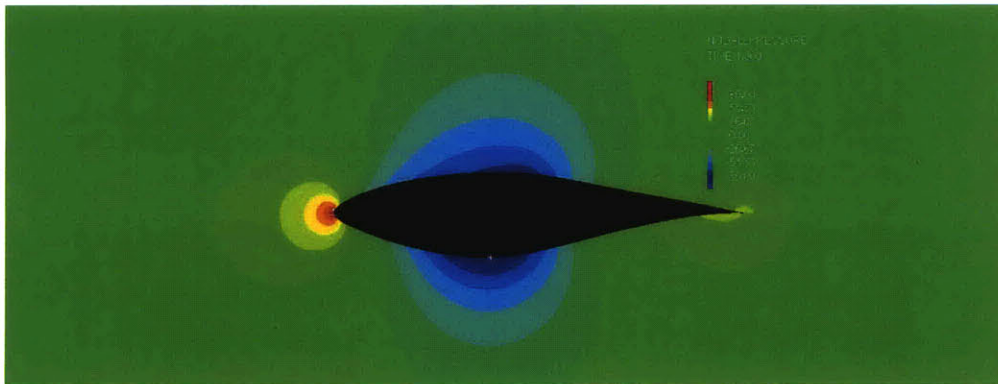


Fig. 17: S809 pressure field at RE=10E6, AoA=0°

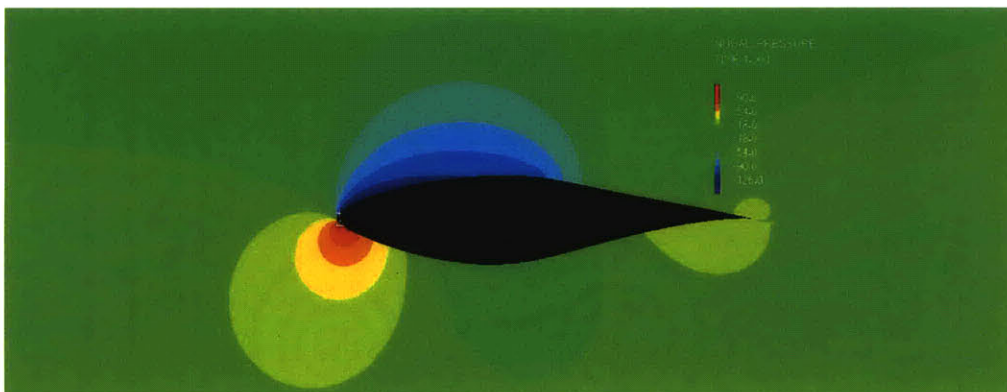


Fig. 18: S809 pressure field at RE=10E6, AoA=6°

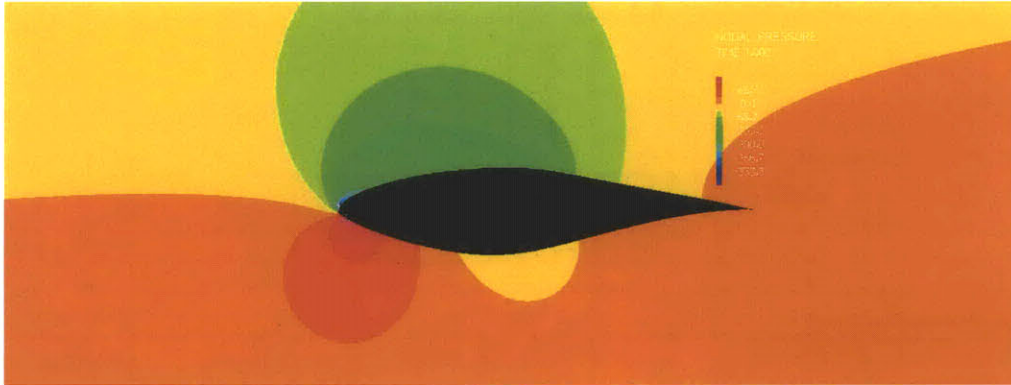


Fig. 19: S809 pressure field at RE=10E6, AoA=10°



Fig. 20: S809 pressure field at RE=10E6, AoA=12°



Fig. 21: S809 pressure field at RE=10E6, AoA=14°

Since the Reynolds number is low, the pressure coefficient equation for incompressible flow can be used (Eq. 6.1). It relates the pressure difference to the dynamic pressure.

$$c_p = \frac{p - p_\infty}{\frac{1}{2} \rho_\infty V_\infty^2} \quad (6.1)$$

In fig. 22 to 26 the pressure coefficients calculated by ADINA but also the results calculated by the Risoe Institute are plotted over the chord length of the foil.

Fig. 22: S809 pressure distribution at $Re=10E6$, $AoA=0^\circ$

S809 AoA 0°

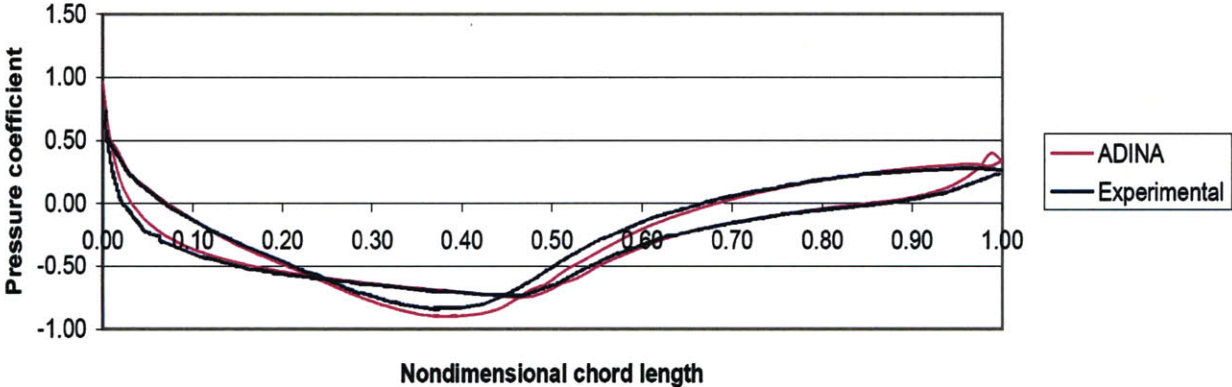


Fig. 23: S809 pressure distribution at $Re=10E6$, $AoA=6^\circ$

S809 AoA 6°

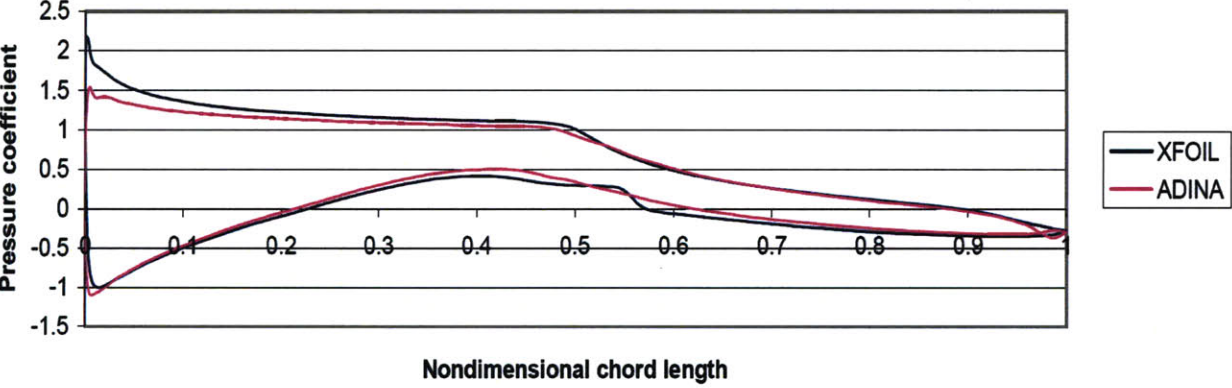


Fig. 24: S809 pressure distribution at $Re=10E6$, $AoA=10^\circ$

S809 AoA 10°

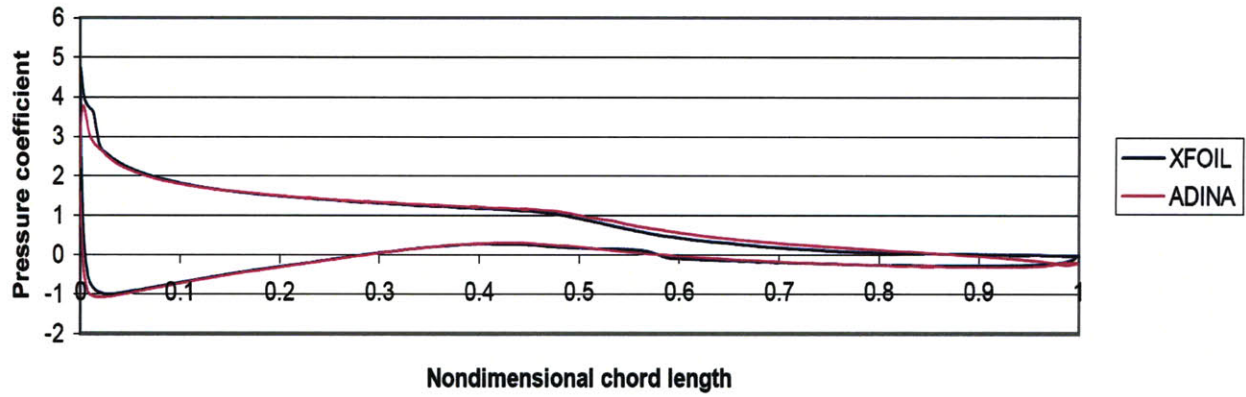


Fig. 25: S809 pressure distribution at $Re=10E6$, $AoA=12^\circ$

S809 AoA 12°

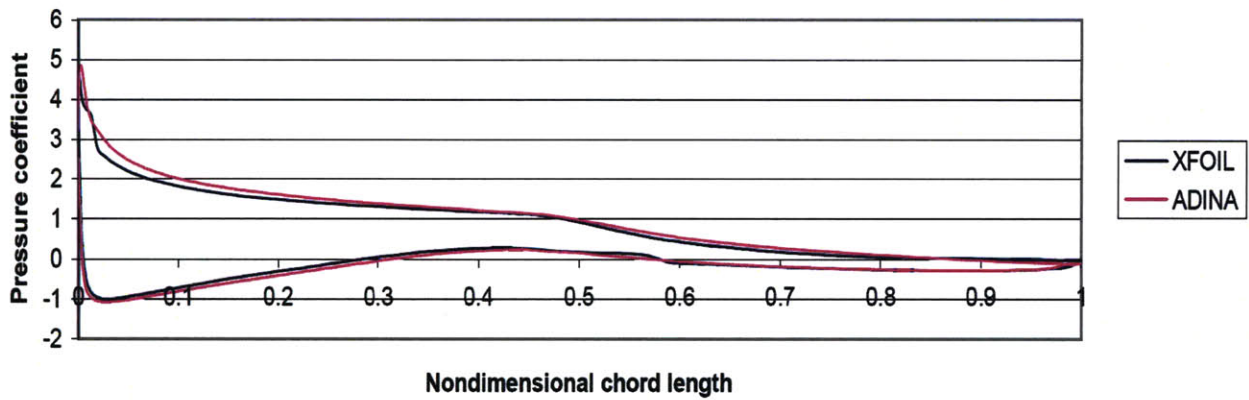
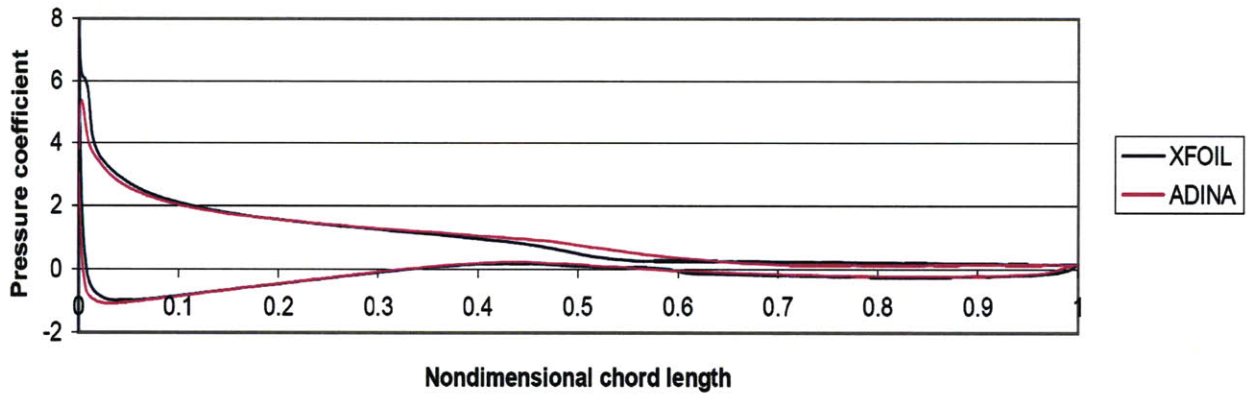


Fig. 26: S809 pressure distribution at $Re=10E6$, $AoA=14^\circ$

S809 AoA 14°



The results show that there is good agreement between the CFD results and experimental data at the angle of 0° . At an angle of attack of 6° the CFD pressure coefficient is about 16% lower than the panel code results in the first 10% of the leading edge. The remaining 90% of the chord length show very exact agreement. With rising angle of attack both simulation tools converge to show even better agreement. Especially at an angle of attack of 12° the two curves match very well. This angle is especially important for further simulations regarding the test turbine, and the results indicate that CFD is appropriate for examinations of the wind turbine.

6.3. Panel code simulations

To enable the simulation of wind turbines in a BEMT code, the airfoil characteristics have to be calculated. For this purpose the 2D inviscid panel code XFOIL is used. XFOIL uses the non-dimensional Reynolds number to describe the geometry of the blade. In turn, this means the number of calculations needed for the simulation of a wind turbine is the number of wind speeds, multiplied by the number of blade segments. Each calculation provides the lift coefficient, the drag coefficient and the pitching moment coefficient over angles of attack from 0° to 20° . Unfortunately, no extensive experimental data of airfoil characteristics for the desired range of Re numbers are accessible. In the wind turbine airfoil catalogue of the Risoe Institute [26] the airfoil characteristics for the S809 shape are given experimentally and calculated with XFOIL for a Reynolds number of $1.00E6$. Additional experimental data of the S809 airfoil at $Re = 1.00E6$ are given in [27], and they are performed by the Ohio State University.

Before building up a database for the wind turbine calculations, XFOIL results are benchmarked against experimental data from above mentioned Institutions.

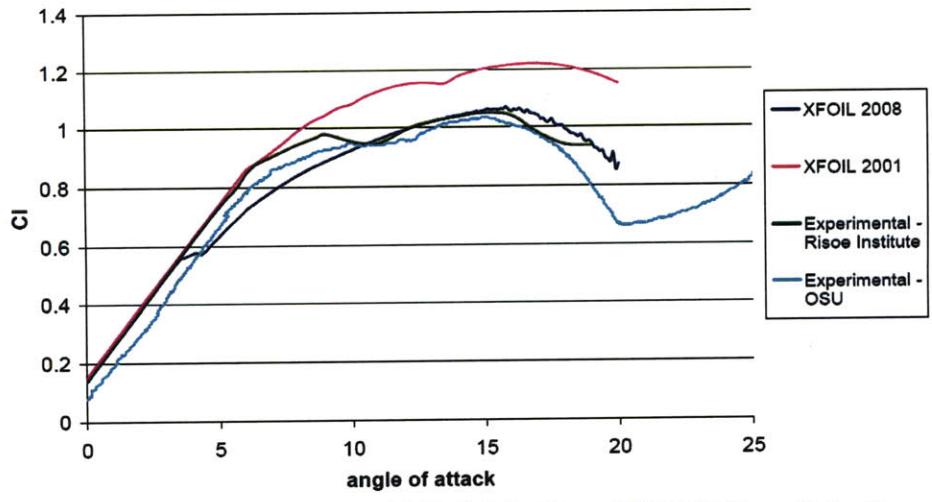


Fig. 27: Benchmark of XFOIL results for the S809 airfoil at $Re = 1.00E6$ (Lift coefficient)

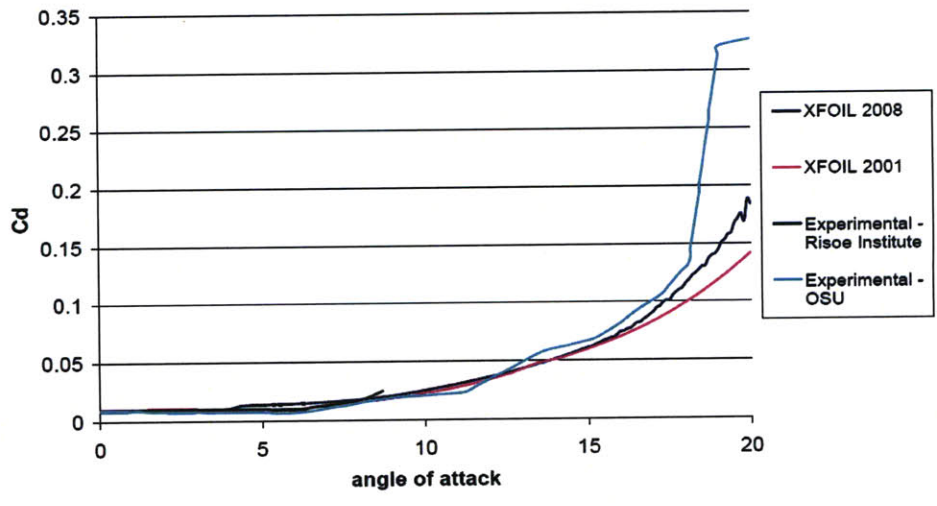


Fig. 28: Benchmark of XFOIL results for the S809 airfoil at $Re = 1.00E6$ (Drag coefficient)

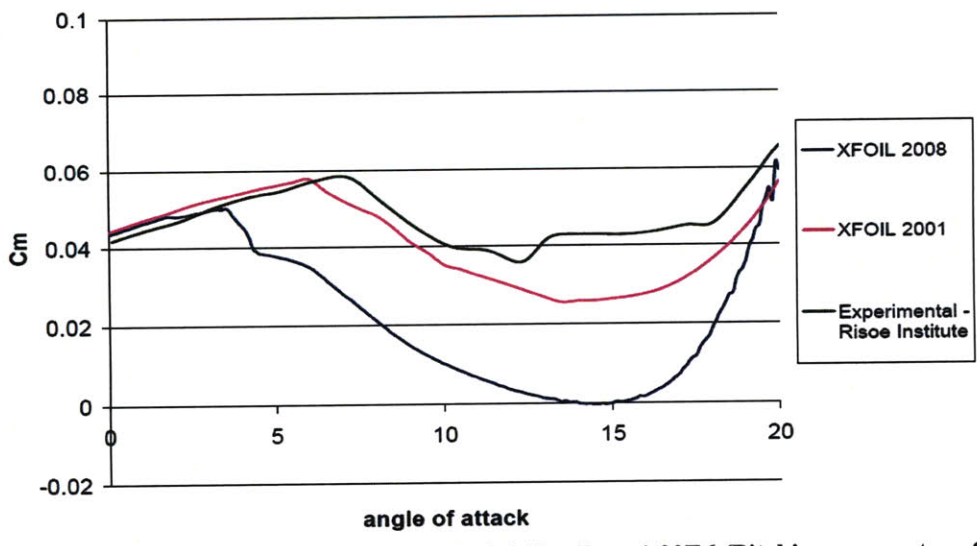


Fig. 29: Benchmark of XFOIL results for the S809 airfoil at $Re = 1.00E6$ (Pitching moment coefficient)

The results of the benchmark of the S809 profile at $Re = 1.00E6$ are presented in Figs. 27-29. Fig. 27 shows that the lift coefficients, simulated by using XFOIL, match quite well with experimental data and it also shows that XFOIL has been improved since 2001. Simulated drag coefficients, shown in Fig. 28 also match quite well with experimental data. Only the pitching moment coefficients (Fig. 29) diverge significantly from experimental data and even from the XFOIL results in 2001. However, the lift and drag coefficients are by far the most important coefficients in wind turbine simulations. Hence the decision is to accept XFOIL results and set up the needed database for all necessary Re numbers by using this panel code.

6.4. Processing a 360° dataset of airfoil characteristics

As described in Ch. 5.1 the calculated airfoil characteristics have to be preprocessed in order to be useful in BEMT codes. The complete process has been performed using the AIRFOILPREP code by NREL. The final results after preprocessing for $Re = 1.00E6$ are exemplary shown in Fig. 30.

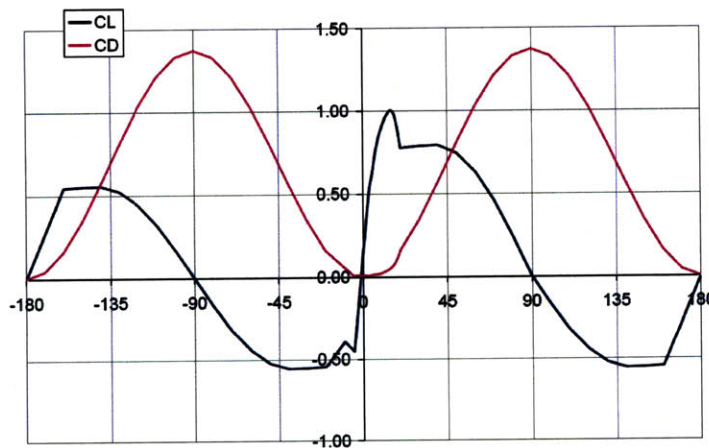


Fig. 30: Preprocessed airfoil data of the S809 profile at $Re = 1.00E6$

7. The NREL phase VI test turbine

7.1. Turbine design and characteristics

The laboratory of the US Department of Energy, NREL, tested a 10-meter diameter research wind turbine (Fig. 31, 33) in the world’s largest 24.4 by 36.6 meter wind tunnel, operated by the NASA in California (Fig. 32). The NREL “Unsteady Aerodynamics” research wind turbine was extensively instrumented to characterize the aerodynamic and structural responses of a full-scale wind turbine rotor. Measured quantities included inflow conditions, airfoil aerodynamic pressure distributions, and machine responses. The turbine was tested in the wind tunnel, in a 2-bladed, fixed-pitch (stall-controlled) configuration. It was operated at constant speed of rotation with the rotor oriented upwind of the tower. An extensive range of pitch angles, pitch motions, yaw positions, and wind velocities were tested. The three-week test was completed in May 2000 with the turbine operated in over 1700 different test conditions. Details on the phase VI turbine experiment can be found in [28].

For the analysis in this thesis only, the steady state conditions at wind velocities from 5 m/s to 25 m/s are considered. Table 9 shows the turbine’s operating conditions and its rotor blade characteristics.



Fig. 31: NREL ph. VI test turbine [74]



Fig. 32: Ames-NASA wind tunnel [74]

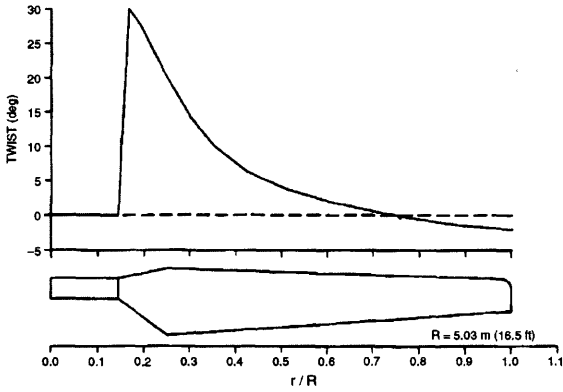


Fig. 33: Chord and twist distribution

Characteristics of operation:		Blade shape distribution		
		r/R	Chord	Twist
Wind velocities:	5 - 25 m/s	0.225	0.737	30
Rotational speed:	72 rpm const.	0.275	0.7116	22.5
Pitch:	Fixed pitch at 3°	0.325	0.6862	15
Load control:	stall controlled	0.375	0.6608	11
		0.425	0.6354	7
Rotor blade characteristics:		0.475	0.61	5.5
		0.525	0.5846	4
Rotor radius:	5 m	0.575	0.5592	3
Number of blades:	2	0.625	0.5338	2
Blade type:	S809	0.675	0.5084	1
		0.725	0.483	0
		0.775	0.4576	-0.5
		0.825	0.4322	-1
		0.875	0.4068	-1.66
		0.925	0.3814	-2.33
		0.975	0.356	-3

Table 9: Operating conditions and rotor characteristics

7.2. Model construction for simulations

To perform the simulation procedure for the design of passively adaptive rotor blades (Fig. 12) for the NREL ph. VI turbine, a blade model of the selected turbine has to be constructed. For the aerodynamic simulation with a BEMT code, as the core part, the model has to be established to be applicable in WT_perf. It consists of a dataset containing rotor design characteristics and the turbine's operating conditions. Upfront the specific airfoil characteristics need to be calculated and preprocessed in XFOIL and AIRFOILPREP. This procedure is discussed in Ch. 6.4.

For the structural simulation process in ADINA, the geometry of the blade's body has to be generated. For this purpose the generalized specifications of the airfoil S809 and the rotor design characteristics are transformed into an ADINA compatible input file using a developed Excel algorithm. The blade is divided into 16 segments. Each cross-section is defined by 65 points equally distributed on the hull of the blade. The overall number of 1040 points is connected by surfaces to create a geometrical model of the blade. Fig. 34 shows this model. The constructed model is a hull created out of shell elements with an equally distributed thickness. Real wind turbine rotor blades are often optimized by varying shell thickness or a supporting inner construction. Hence the model used for simulations is a first simplified approach in a blade design process.

ADINA

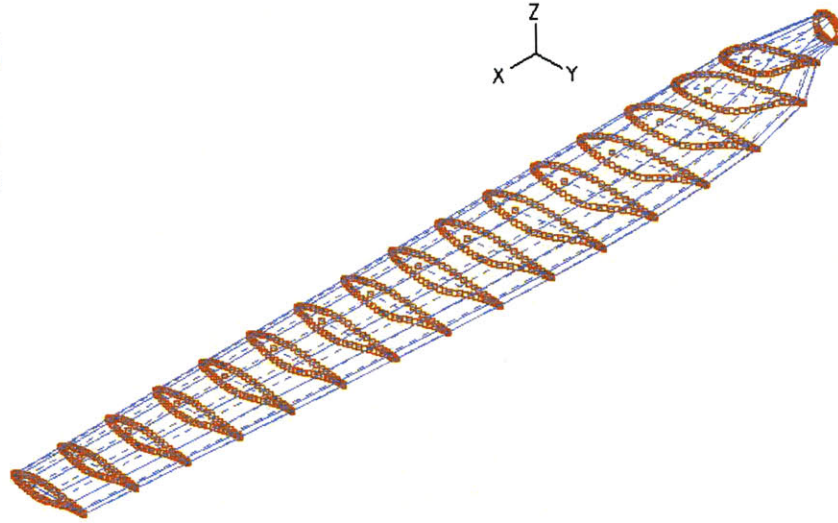


Fig. 34: Model of the phase VI wind turbine to be used in ADINA

As discussed in Ch. 2.2.1, lift and drag forces as well as pitching moments act around the point of attack at one quarter of the chord length. For this reason rigid beams that represent the chord line have been added to each cross-section. The geometries and forces are shown in Fig.35.

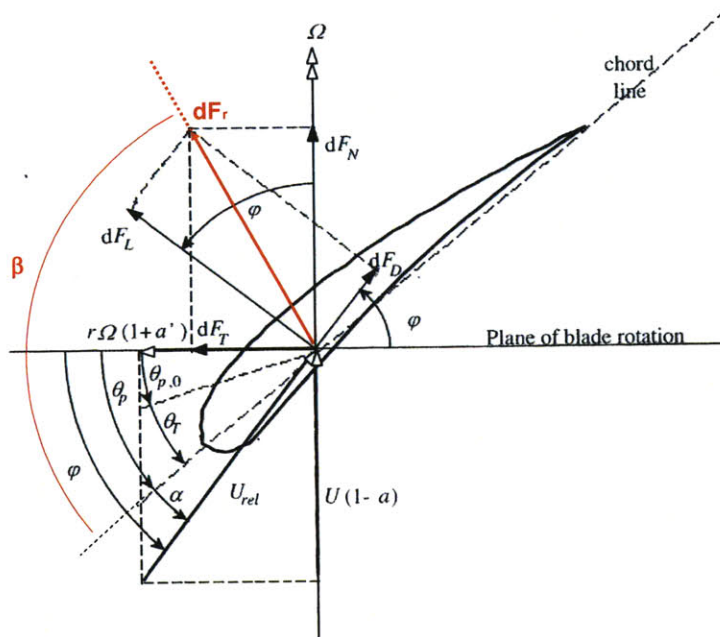


Fig. 35: Sketch of aerodynamic forces attacking a blade segment (adapted from [13])

In the output file of WT_perf the aerodynamic forces are given in terms of thrust force (dF_N) and torque forces (dT). Since both forces attack the airfoil cross-section at the same point, they have been merged as the vector product (dFr) and the angle between this resulting force and the chord line is defined as (β). In the model the forces attack at the outer side of each blade segment.

7.3. Verification of aerodynamic simulation results

The given wind turbine’s operational characteristics and the created datasets on aerodynamic behavior of the rotor blades enable a performance simulation using the blade element momentum theory (Ch. 2.2.3). The BEMT code WT_perf has been chosen for this procedure. In the same way as spot tests of the calculation of airfoil characteristics have been carried out against experimental data, the total aerodynamic simulation tool is benchmarked against experimental data as well as against a simulation, where an older version of WT_perf was used in 2002 [77]. In Fig. 36 the simulation results performed in 2008 show quite good agreement with the experimental results of the phase VI turbine obtained in the wind tunnel experiments. The simulation differences of the two different WT_perf results can imply how the code has been improved during the last years. On the other hand, it is also possible that the used input data in this work are more accurate and hence cause the improvement.

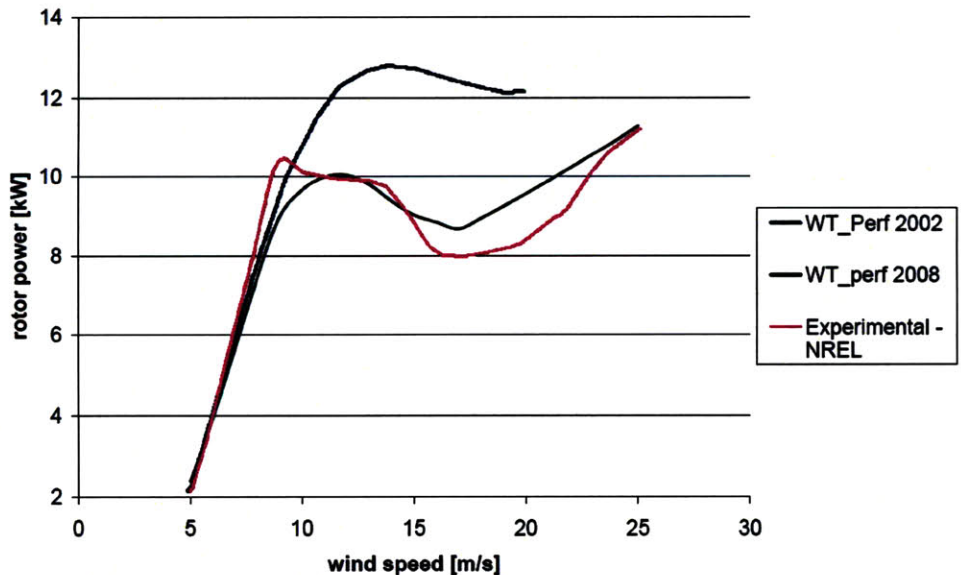


Fig. 36: Benchmark of WT_perf simulations of the phase VI turbine against experimental data

8. Aeroelastic tailoring to optimize the NREL test turbine

8.1. Aerodynamic optimization of the blade profile

The NREL phase VI turbine, and other turbines operating under similar conditions, can be optimized in the following ways. To respond more efficiently to the physics of the optimal flow field, discussed in Ch. 2, an enhanced rotor control using variable speed and blade pitch control mechanisms can easily optimize the power curve shown in Fig. 36. The increased complexity of the turbine on the other hand is usually only profitable for larger wind turbines. A deeper analysis of the blade shape itself might also show optimization potential for the rotor's efficiency. The original chord of the phase VI turbine has a linear distribution. Chapter 4.2 shows how the optimal chord distribution can enhance the rotor efficiency.

Another optimization possibility is the adaptation of the blade's shape to changing wind and operating conditions in order to approach the optimal profile and especially the optimal angle of airflow attack. This blade deformation can have two aims: (1) reducing loads by improving stall mechanisms and hence permitting larger rotors, (2) increasing power efficiency by adjusting to the optimal angle of attack. The developed procedure (Fig. 12) is designed to analyze the optimization option (2), but can also be adjusted to design adaptive rotor blades which reduce loads, option (1).

8.1.1. Potential power enhancement

The aerodynamic simulation of each rotor blade segment over the range of operating conditions has been performed as shown in Fig. 12. In this case, the turbine is segmented into 16 parts. Angles of attack were analyzed from -5° to 25° for 5 wind velocity steps (5, 7, 9, 11, 13 m/s). Hence the WT_perf code has to be run in 2400 cases and delivers performance and load results for each case. A simple optimization algorithm seeks for the optimal angle of attack at each section for each wind speed and provides the related power and load values. Integration over the individual segment results provides the optimized power curve as shown in Fig. 36. The visualization of the calculated improvement results can not be seen clearly when plotting them in Fig. 36. Hence, the improvement for each considered wind speed is shown in Table 10. The table

on the one hand shows the efficiency improvement which can be achieved using a global pitch control, like those used for large turbines; on the other hand it shows the improvement of an optimal non-linear adaptive blade. The upgrade potential of a pitch controlled turbine is also given in the table. Since the phase VI turbine is designed to start stalling at the rated power (in the range of wind velocities of 11 m/s) in order to keep loads at a decent level, only the improvement potential before reaching rated power, P_N , should be considered.

Table 10: Efficiency improvement of the ph. VI turbine in % (pitch control, optimal adaptivity)

Wind velocity	Variable blade pitch control	Optimal adaptive blade	Optimal adaptive blade in addition to variable pitch control
5 m/s	0.728	5.653	4.889
7 m/s	1.879	2.799	0.903
9 m/s	1.180	2.925	1.724
11 m/s	21.844	28.142	5.169

The results of the aerodynamic simulation of passively adaptive blades (for the phase VI wind turbine) show that a variable pitch control of the rotor blades can improve its efficiency by 1% to 2% in the wind range of 5 to 9 m/s. An optimal adaptive rotor blade on the other hand, has the potential to improve the rotor by 3% to 5%. An optimal adaptive blade in addition to a variable pitch control has the possibility to further enhance the overall efficiency.

8.1.2. Optimal blade deformation

The calculated power enhancements for optimal adaptive blades (shown in Table 10) were achieved by continuously adapting each blade segment to the optimal angle of airflow attack. For the case of the ph. VI turbine, the optimal angle of attack increases with rising wind velocities. The physical explanation is that the angle between the airflow and the plane of rotation, φ , becomes larger with rising wind velocities, since the turbine operates at a constant rotational speed. A pitch control system has the ability to partly react on the angular change. The simulation results (Fig. 37) shows how the pitch angle has to increase for power enhancement.

A simulation analysis of the optimal AoA values of each blade segment of the VI turbine shows that the optimal AoA should increase stronger at the blade hub than at the blade tip. For this case, the blade is regarded as if each blade segment is fully twistable against its bordering segments, representing an optimal adaptive blade.

This optimal behavior of such a blade assumption is shown in Fig. 38. It is quite clear that the calculated optimal adaptation is hardly possible to be achieved in practice by using passive adaptation methods based on material properties.

On the other hand, an adaptive blade in addition to a global pitch control mechanism still has further improvement potential as the results in Table 10 show.

The desired blade deformation needed for this case (Fig. 39) shows that this behavior can most probably be achieved using induced material deformations. The graph illustrates how the pitch angle has to continuously decrease from the rotor hub to the tip with higher wind speeds.

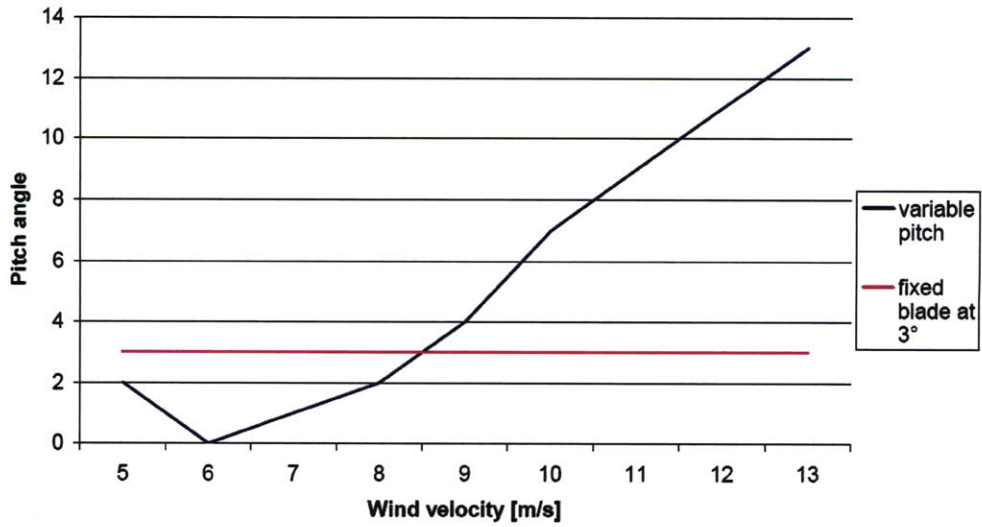


Fig. 37: Optimal variation of the global pitch angle

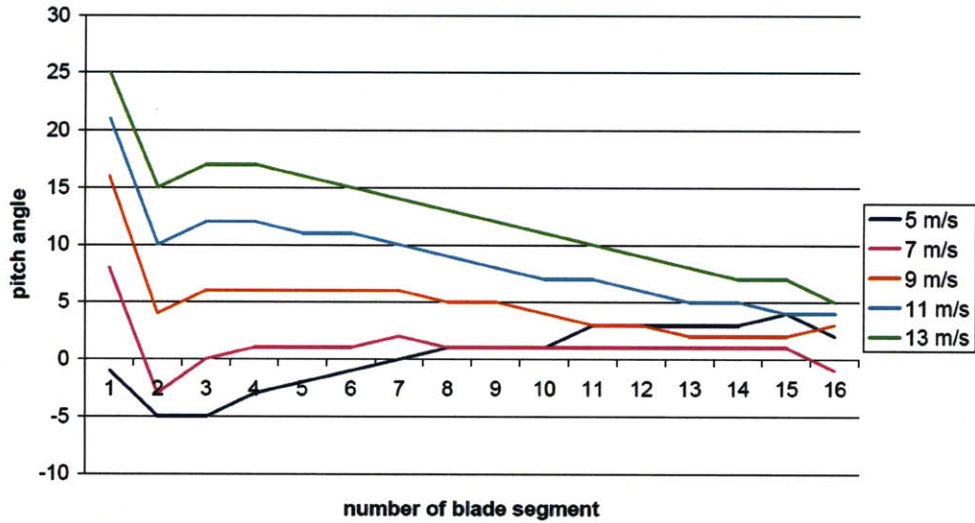


Fig. 38: Optimal deformation of an adaptive rotor blade

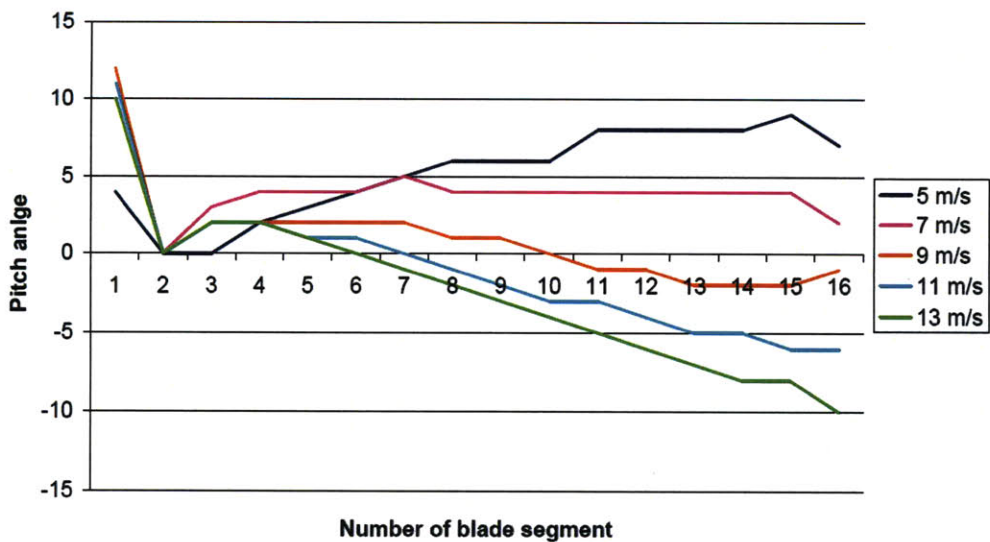


Fig. 39: Optimal deformation of an adaptive rotor blade in addition to a pitch control system

8.1.3. Aerodynamic loading

The loading onto the rotor blade consists of the partial thrust forces, dF_N and the partial force which create the torque around the rotational axis, dT . As was discussed in previous chapters, both forces attack the airfoil shape after the first quarter of the chord line and have been merged to the resulting force, dF_r , at the angle, β , measured from the chord line (Fig. 35). The aerodynamic loading on the rotor blade for the simulations that were carried out is shown in Fig. 40. The corresponding angles, β , are shown in Fig. 41. The force vectors attacking the actual blade model in ADINA are shown exemplary for the case of a wind velocity of 9 m/s in Fig. 42.

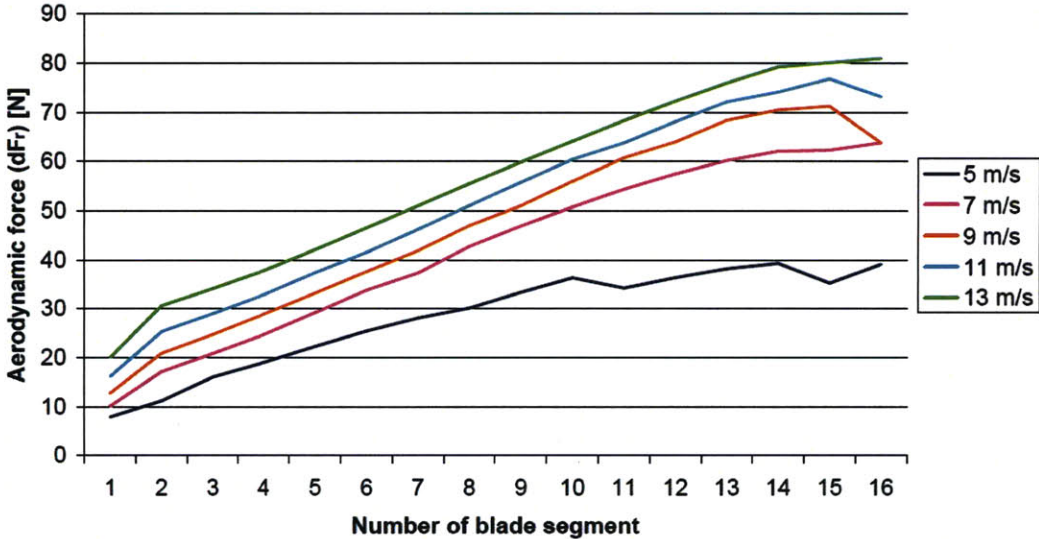


Fig. 40: Aerodynamic loading on the rotor blade (dF_r)

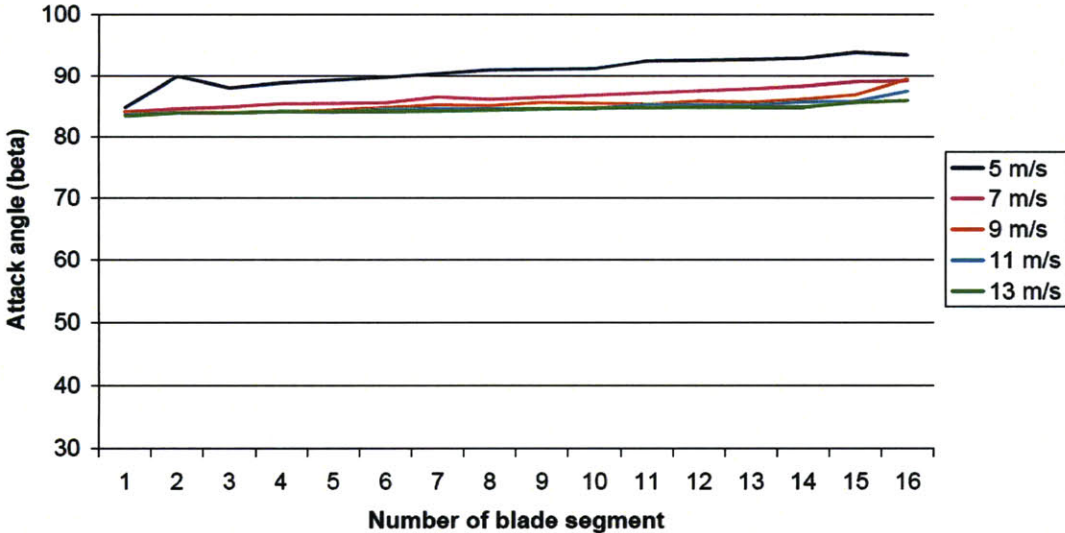


Fig. 41: Angles of force attack (β)

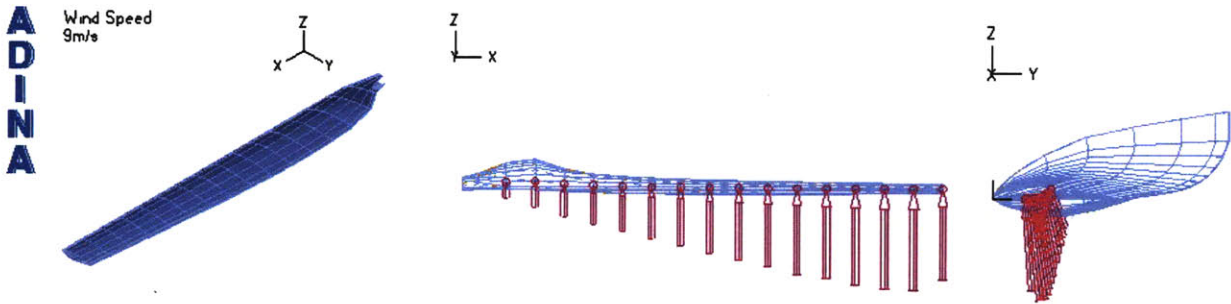


Fig. 42: Force vectors attacking the ADINA blade model at a wind velocity of 9 m/s

8.2. Structural simulation of blade profile deformations

8.2.1. Material design

The hypothesis, orthotropic material characteristics create bend-twist effects, has been set up and experimentally shown in Ch. 5.3. In the same chapter there is evidence that material characteristics of a flat beam in the third dimension - perpendicular to the surface - have a negligible effect on bend-twist material properties. Hence the 2D simulation code LAMICENS can be used to simulate suitable composite materials.

Based on these facts, the first approach was to find a composite material using LAMICENS that has the strongest orthotropic material characteristics (Material #1 in table 11). The composite material (#1) consist of 250g/m^2 - carbon fibers with 40% volume share in an L100/EPH294 resin matrix. In order to have a comparable isotropic material, similar fiber and matrix types have been arranged to create homogeneous properties in all two dimensions (Material #2 in table 11). The composite material (#2) consists of three layers of 204g/m^2 - carbon fiber textures at the angles 0° , 30° , 60° . Each layer has a volume share of 20% in an L100/EPH294 resin matrix.

For orthotropic material simulations in ADINA, material characteristics in the third dimension are also necessary. The designed material (#1) has only one fiber direction and a homogeneous matrix. Hence the material characteristics perpendicular to the fiber direction are also applicable in the third dimension. Figs. 43 and 44 graphically show the material simulation results, performed in LAMICENS.

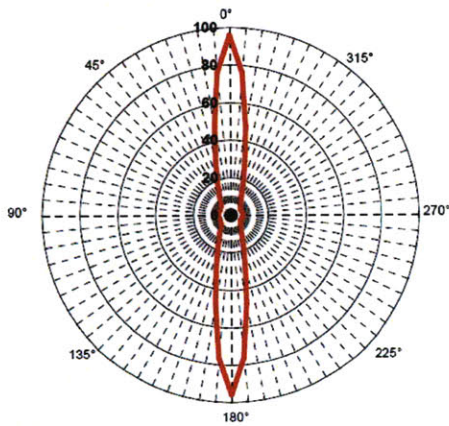
Table 11: Simulated material characteristics

Material #	Type	Axis	Young's modulus	Axis	Poisson ratio	Axis	Shear modulus
1	Orthotropic	a	95 Gpa	ab	0.48	ab	6 Gpa
		b	10 Gpa	ac	0.48	ac	6 Gpa
		c	10 Gpa	bc	0.1	bc	2.7 GPa
2	Isotropic	all	19 Gpa	all	0.32	all	7.4 Gpa

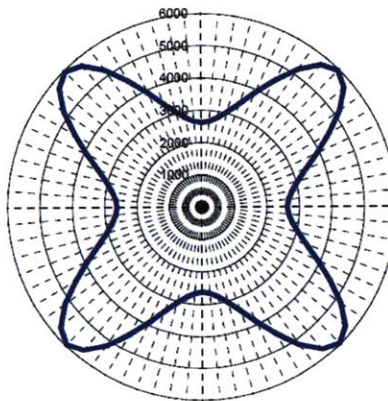
Table 12: Material configurations

Configuration #	Material #	Shell thickness	
		D1	D2
1		1 0.0300 m	-
2		2 0.0300 m	-
3		1 0.0100 m	-
4		2 0.0100 m	-
5		1 0.0050 m	-
6		2 0.0050 m	-
7		1 1.0000 m	-
8		2 0.0005 m	0.05 m
9		1 0.0005 m	0.05 m
10		2 0.0040 m	0.02 m
11		1 0.0040 m	0.02 m

Young's modulus in GPa



Shear modulus in GPa



Poisson ratio

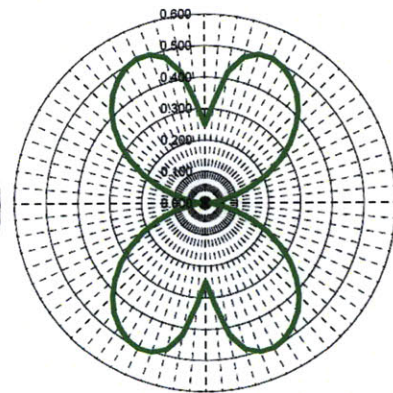


Fig. 43: LAMICENS simulation visualization of material characteristics (Material #1)

Young's modulus in GPa

Shear modulus in GPa

Poisson ratio

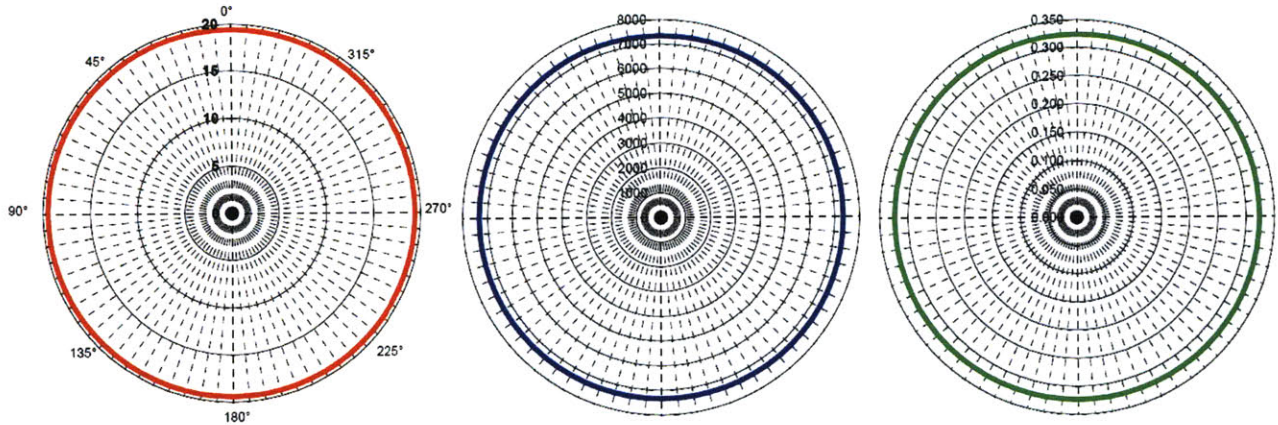


Fig. 44: LAMICENS simulation visualization of material characteristics (Material #2)

8.2.2. Structural design and simulation

The design procedure (Fig. 12) shows the necessary components for a structural simulation in ADINA based on FEM. These components are the original blade model (Ch. 7.2), the results concerning desired deformation and load changes from the aerodynamic simulation (Ch. 8.1) and material characteristics (Ch. 8.2.1).

8.2.2.1. Constant shell thickness

In the first round of structural simulations, the thickness of the blade shell is assumed to be constant everywhere. Table 12 shows the thicknesses D_1 (Fig. 45) for the different runs. The material properties which are investigated are given in Table 11.

Figs. 46 - 48 show the corresponding simulation results and how the blade deforms.

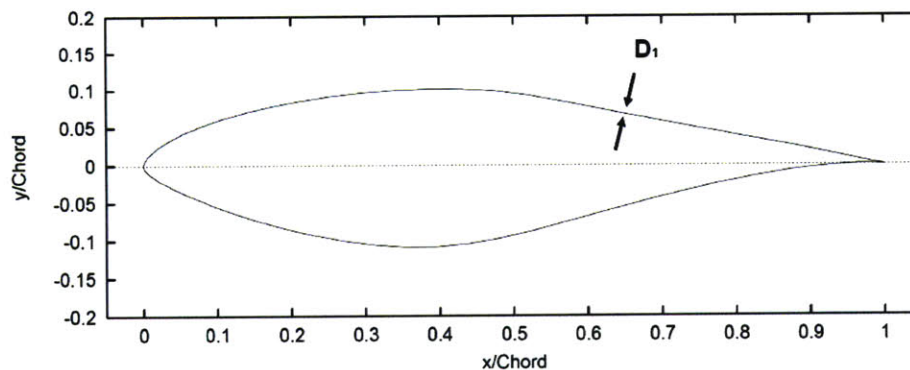


Fig. 45: S809 airfoil shape, constant thickness D_1

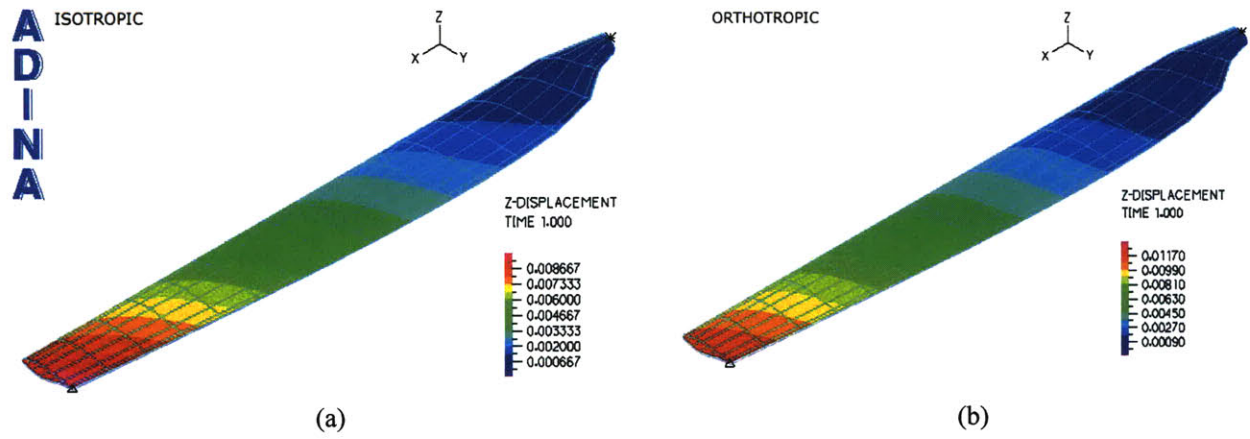


Fig. 46: Structural response simulation for material configurations (a) = Material #2, (b) = Material #1

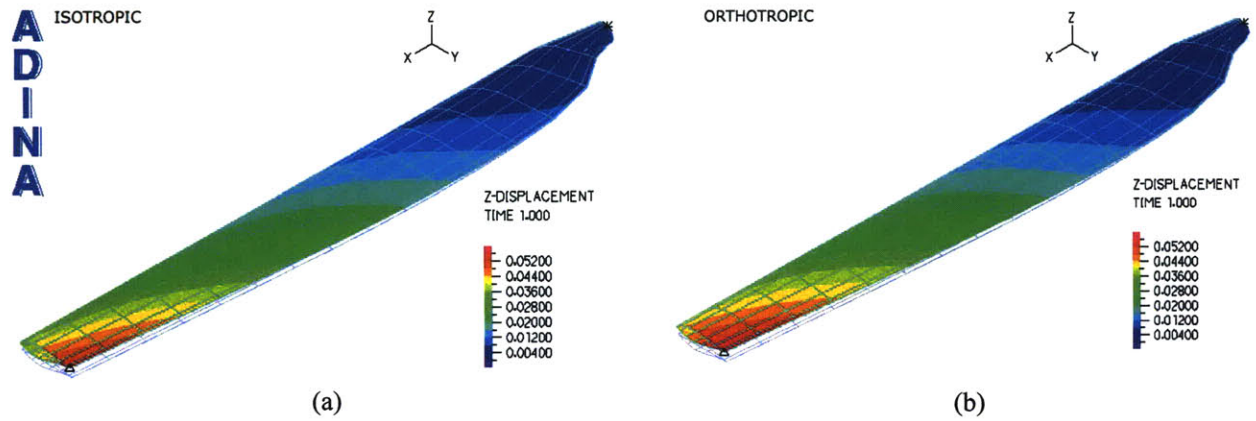


Fig. 47: Structural response simulation for material configurations (a) = Material #4, (b) = Material #3

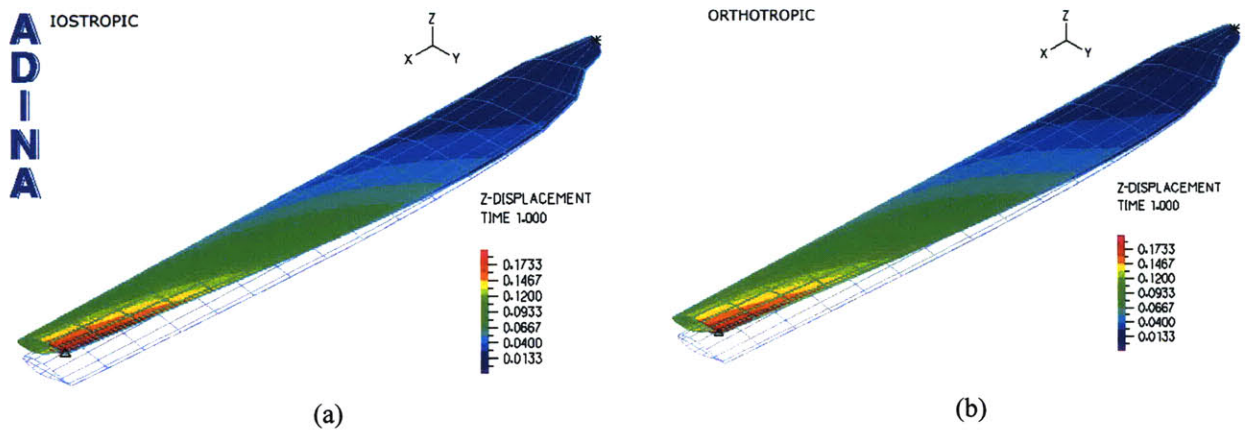


Fig. 48: Structural response simulation for material configurations (a) = Material #6, (b) = Material #5

By geometrically comparing the displacements of the leading edge and the trailing edge at zero wind velocity and at the considered wind velocity the twisting of the blade can be calculated for each blade segment. The nominal twist effect of blade segment 8 and 16 as well as the differences between isotropic materials and orthotropic materials can be seen in Table 13 for the case of a wind velocity of 9 m/s.

Table 13: Calculation of the rotor twist for segment 16 and segment 8 at a wind speed of 9 m/s

Segment 16						
Material configuration	Displacements			Twist		
	Node 263	Node 255	Difference	Nominal	Difference	Demanded
1 (isotropic)	0.009	0.010	0.001	0.198°		-9°
2 (orthotropic)	0.011	0.012	0.001	0.154°	-0.044°	-9°
3 (isotropic)	0.035	0.056	0.021	3.377°		-9°
4 (orthotropic)	0.041	0.057	0.016	2.552°	-0.824°	-9°
5 (isotropic)	0.085	0.197	0.112	17.472°		-9°
6 (orthotropic)	0.098	0.188	0.090	14.166°	-3.306°	-9°

Segment 8						
Material configuration	Displacements			Twist		
	Node 135	Node 127	Difference	Nominal	Difference	Demanded
1 (isotropic)	0.0033	0.0040	0.0007	0.119°		-5°
2 (orthotropic)	0.0041	0.0048	0.0006	0.098°	-0.021°	-5°
3 (isotropic)	0.0136	0.0239	0.0103	1.663°		-5°
4 (orthotropic)	0.0158	0.0239	0.0080	1.291°	-0.371°	-5°
5 (isotropic)	0.0342	0.0839	0.0497	7.949°		-5°
6 (orthotropic)	0.0381	0.0783	0.0401	6.430°	-1.519°	-5°

The selected results at blade segment 8 and 16 for a wind speed of 9 m/s show that the rotor blade of the NREL ph. VI turbine, modeled as a hull of equally distributed thickness does not twist to the optimal shape by using orthotropic composite materials. In fact, the blade twists in the opposite direction for isotropic as well as for orthotropic material properties. Nevertheless the orthotropic material twists less against the optimization direction and hence the use of orthotropic composite materials will improve the efficiency of the ph. VI wind turbine. The reason for the twist in positive direction of β , is the geometrical moment of inertia and the torsional rigidity of the blade's geometry.

Table 13 also shows that the twisting amount of the blade is proportional to the bending amount, depending on the amount of the node displacements. Hence a thinner hull results in a higher twist and it also increases the difference in blade twist between isotropic and orthotropic materials.

8.2.2.2. Investigation of structural design effects

The first round of structural blade simulations with a constant shell thickness revealed that the use of orthotropic material design enable systematic aeroelastic tailoring. However, the moment of inertia of the structure is critical. Having a constant shell thickness the deformation is opposite to the required direction.

In two experiments the effects of orthotropic properties but also the effects of redesigning the moment of inertia are investigated. Fig. 49 shows a theoretical model with an imaginary shell thickness of 1m. Practically, this is impossible, but the result shows that strong orthotropic effects will outperform the moment of inertia.

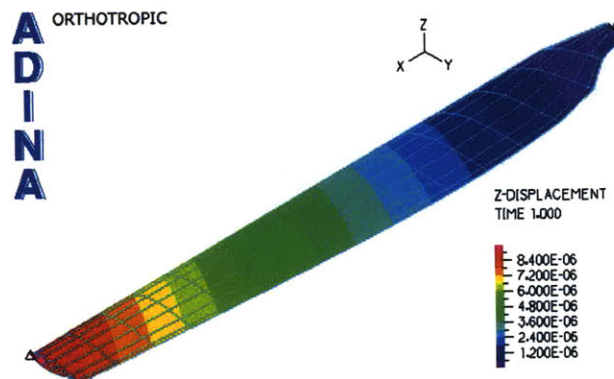


Fig. 49: Structural response simulation for material configurations #7

In the second experiment (Fig. 50) the thickness of the blade at the trailing edge (D_2) is set to 5cm and at the leading edge (D_1) it is set to 5mm. This offset aims to balance the change in thickness of the blade itself.

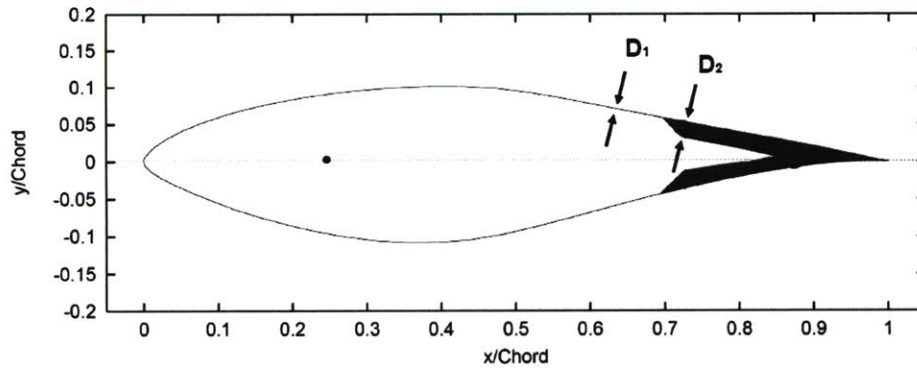


Fig. 50: S809 airfoil shape, two areas of thickness

The deformations (Fig. 51, 52) show that the blade now bends towards stall and therefore improves the turbine’s efficiency. The actual magnitude is shown in table 14.

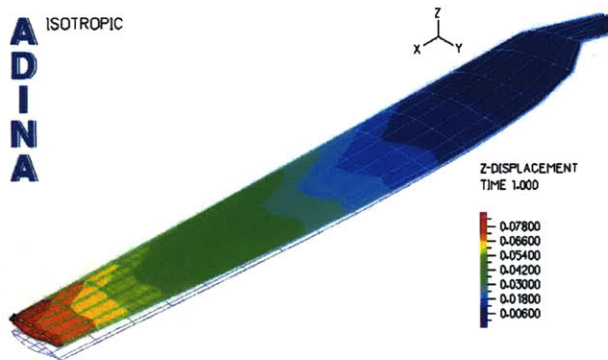


Fig. 51: Structural response simulation for (# 8)

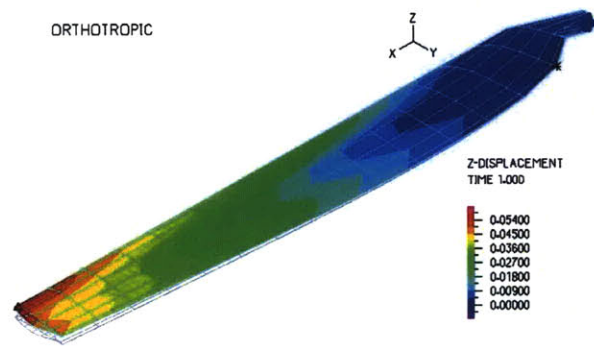


Fig. 52: Structural response simulation for (# 9)

Table 14: Calculation of the rotor twist for segment 16 and segment 8 at a wind speed of 9 m/s

Segment 16					
Material configuration	Displacements			Twist	
	Node 263	Node 255	Difference	Nominal	Demanded
8 (isotropic)	0.0478	0.0368	-0.0110	-1.774°	-9°
9 (orthotropic)	0.0573	0.0453	-0.0120	-1.927°	-9°

Segment 8					
Material configuration	Displacements			Twist	
	Node 135	Node 127	Difference	Nominal	Demanded
8 (isotropic)	0.0281	0.0226	-0.0055	-0.878°	-5°
9 (orthotropic)	0.0255	0.0184	-0.0070	-1.130°	-5°

The change in the thickness has a positive effect on the blade twist. However Fig. 52 also shows that the abrupt jump in the shell thickness leads to non-uniform body deformations. These are not tolerable in practice since they affect the aerodynamic shape of the airfoil geometry.

8.2.2.3. Optimization of the structure

The above experiments have shown positive and negative sides of structural design effects for wind turbines. The theoretical knowledge and the experience from simulation results have been used to design the best possible blade structure which is practically realistic.

The goal is to design a blade that shows the largest twist towards stall but also deforms smoothly and does not change the shape of the airfoil geometry.

Experiments of constant shell thickness have shown that thin orthotropic structures bend the most and have therefore the strongest effect in deformation towards stall. Further investigations have proven that a thicker trailing edge will also result in a blade twist towards stall, but abrupt and extreme changes in thickness are not practical.

Fig. 53 shows the optimized blade structure with a smooth crossover of the two thickness sections. The thin section, D_1 , has a value of 4 mm and the thick section, D_2 , has a value of 2 cm.

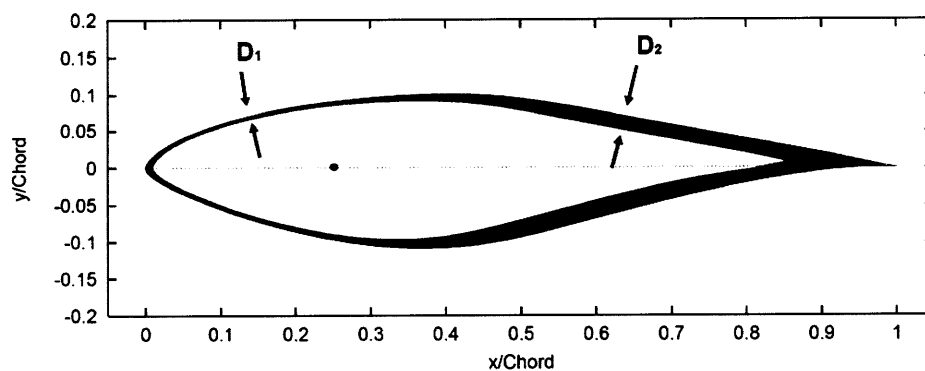


Fig. 53: S809 airfoil shape, two transitioning thickness areas

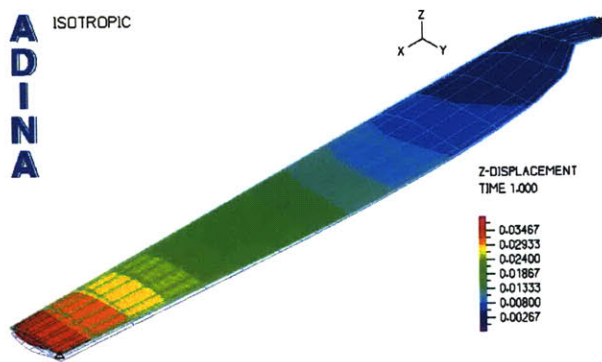


Fig. 54: Structural response simulation for (# 10)

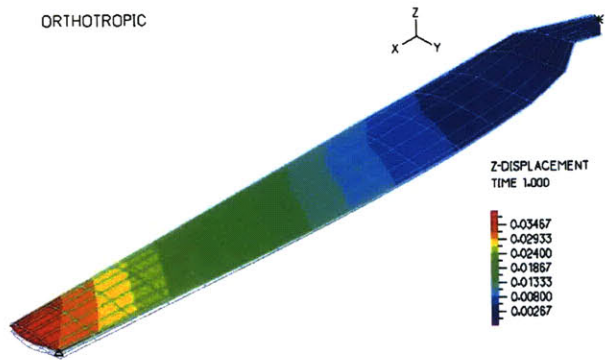


Fig. 55: Structural response simulation for (#11)

The behavior of the optimized structure (Fig. 55) conforms to all requirements for a practical passively adaptive rotor blade. The twist angles are shown in table 15.

Table 15: Calculation of the rotor twist for segment 16 and segment 8 at a wind speed of 9 m/s

Segment 16					
Material configuration	Displacements			Twist	
	Node 263	Node 255	Difference	Nominal	Demanded
10(isotropic)	0.0344	0.0338	-0.0005	-0.087°	-9°
11(orthotropic)	0.0366	0.0319	-0.0047	-0.751°	-9°

Segment 8					
Material configuration	Displacements			Twist	
	Node 135	Node 127	Difference	Nominal	Demanded
10(isotropic)	0.0136	0.0131	-0.0005	-0.088°	-5°
11(orthotropic)	0.0139	0.0106	-0.0033	-0.529°	-5°

The twisting towards stall of 0.75° (segment 16) does not seem to be much. However, the standard blade (number 5 in table 13) twists towards feather by 17.5° in the same segment. That means the improved blade design actually achieves an improvement of 18.25° at the outer part of the blade length.

8.3. Analysis of FSI coupling effects

The power enhancement potential of passively adaptive rotor blades and its design has been examined. The procedure however does not consider the coupling between blade deformation and change in aerodynamic loads. These effects might be small but will be examined by a fluid structure interaction analysis of a 2D cross section of the rotor blade. The results can be transformed into a correction factor in the procedure to take coupling effects into account. The most comprehensive design tool would be based on a full 3D FSI analysis.

8.3.1. The 2D model of a blade cross-section

For the 2D FSI analysis, the cross-section at 85% of the blade length has been chosen exemplarily. This section is cut free for the simulation and is fixed by horizontal, vertical and torsional springs (Fig. 56). Due to the springs which represent the stiffness of the actual 3D blade body at the chosen cross section, the FSI simulation will reveal the discussed coupling effects.

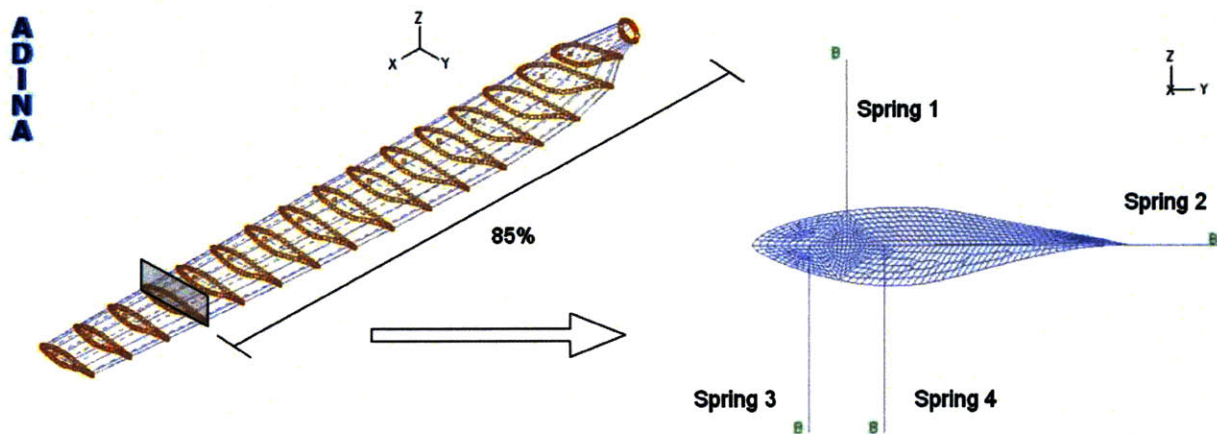


Fig. 56: Reducing the 3D structure into 2D cross-sections

8.3.2. Stiffness properties

A major requirement to carry out the 2D FSI simulation is the determination of the stiffness properties at the selected cross section. A simple model has been developed to determine the properties of the rotor blade at the cross-section which can further be converted into spring constants for the 2D model.

In the assessment the structure of the blade is loaded with the aerodynamic forces along the blade. Then the displacements at each cross-sections are measured individually. Fig. 57 shows this procedure schematically.

The forces and the displacements at the selected section give the stiffness coefficients which exactly represents the behavior of the blade segment under the total aerodynamic loading for one operating condition of the wind turbine (Eq. 8.1 to 8.3).

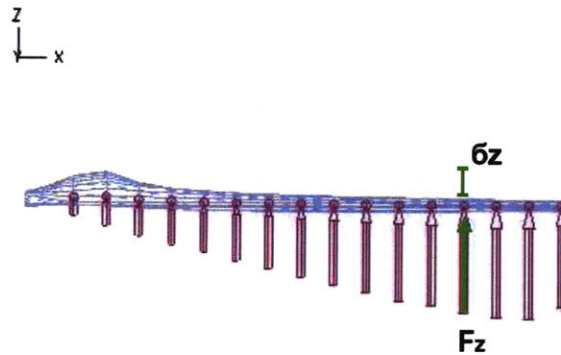


Fig. 57: Model to examine stiffness properties of the structure

$$K_y = \frac{F_y}{\delta y} \quad (8.1)$$

$$K_z = \frac{F_z}{\delta_z} \quad (8.2)$$

$$K_\theta = \frac{M_x}{\delta\theta_x} \quad (8.3)$$

$$K_1 = K_z - (2 * K_3) \quad (8.4)$$

$$K_2 = K_y \tag{8.5}$$

$$K_3 = \frac{2 * K_\theta}{L^2} \tag{8.6}$$

The calculated rotor blade stiffness is converted into spring constants for the FSI model (Eq. 8.4 to 8.6). The rotational stiffness is represented by two standard springs which are attached to the rigid foil at a certain distance from the center of rotation. It needs to be considered that these spring constants (3, 4) not only create a rotational stiffness but also have an effect in the z-direction and hence need to be subtracted from the spring constant in the z-direction (K1).

The distance between the body attachment of springs (3, 4) and the center of rotation needs to be chosen in such way that the 2 x K₃ is always smaller than the respective spring constant K₁. In this case the length has been chosen to be 5 meters.

Fig. 58 to 60 show the blade stiffness properties across its length and table 16 shows the corresponding conversion into the spring constant for the model at 9m/s of wind speed.

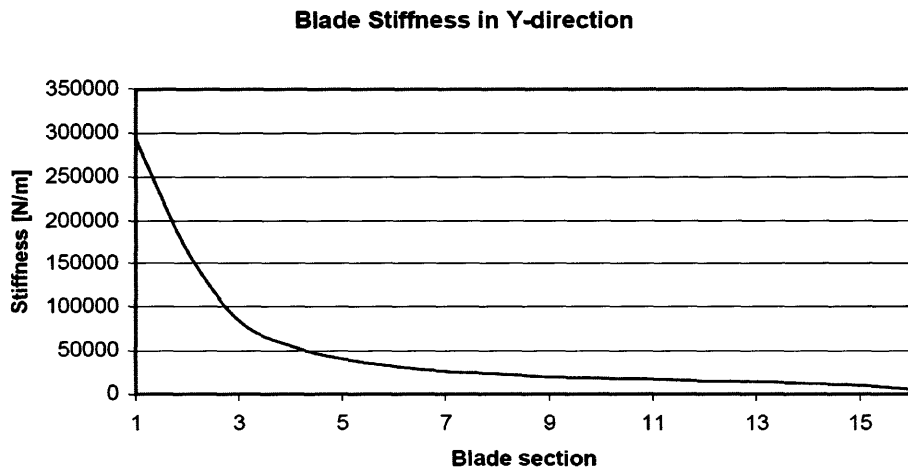


Fig. 58: Blade stiffness in Y-direction

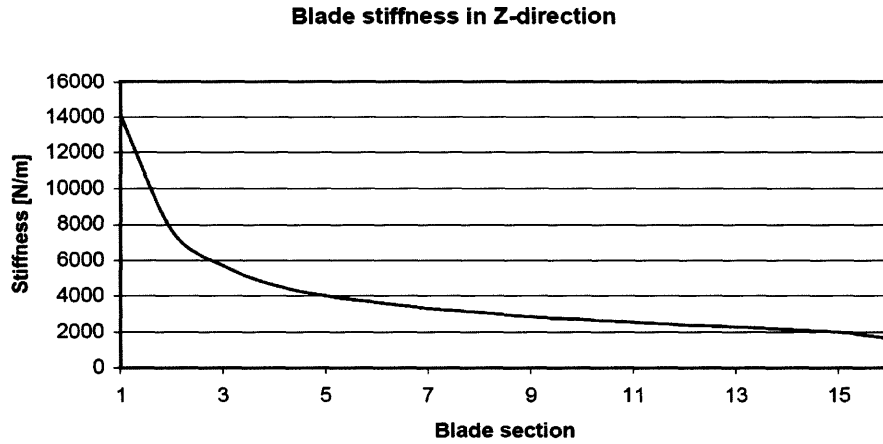


Fig. 59: Blade stiffness in Z-direction

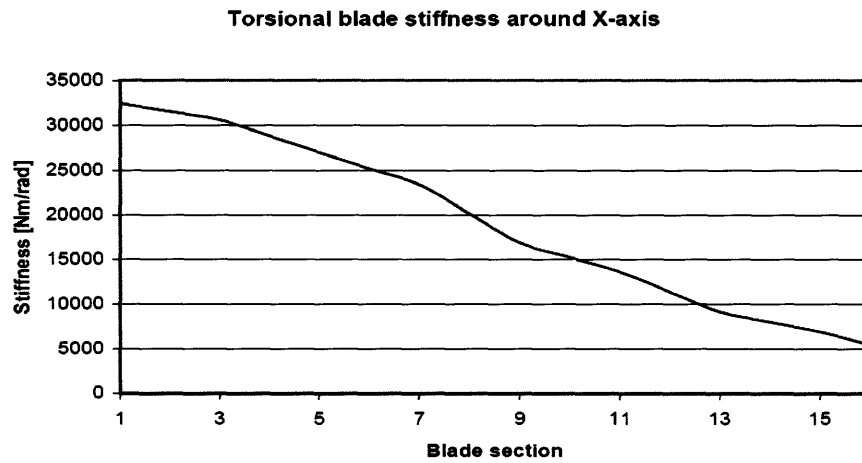


Fig. 60: Torsional stiffness around the X-axis

Table 16: Spring constants

Segment	Rotor blade stiffness			Spring constants for the model		
	Ky [N/m]	Kz [N/m]	K(theta) [Nm/rad]	K1 [N/m]	K2 [N/m]	K3 [N/m]
1	292379	14060	32398	12764	292379	648
2	163963	7643	31496	6383	163963	630
3	84252	5678	30594	4454	84252	612
4	55202	4583	28791	3432	55202	576
5	40538	4000	26988	2921	40538	540
6	31950	3627	25184	2620	31950	504
7	25971	3284	23381	2349	25971	468
8	23243	3064	20131	2258	23243	403
9	19745	2822	16882	2147	19745	338
10	18399	2667	15237	2057	18399	305
11	17366	2533	13591	1989	17366	272
12	15111	2368	11374	1913	15111	227
13	14434	2267	9157	1901	14434	183
14	12355	2119	8032	1797	12355	161
15	10109	1958	6908	1682	10109	138
16	5150	1622	5494	1402	5150	110

8.3.3. FSI analysis

In order to examine the aerodynamic structural coupling effects of the bend twist adaptive rotor blades, an FSI analysis is performed. This analysis aims to investigate the magnitude of these coupling effects and to integrate these results in a correction loop into the design procedure.

Table 17 shows the conditions applied in the analysis.

Table 17: Simulation conditions

Wind speed	9 [m/s]	Air density	1.204 [kg/m ³]
Rotational speed	72 [rpm]	Dynamic viscosity	1.8*10 ⁻⁵ [kg/s*m]
Cross-section: r/R	85%	Chord length	0.4195m
Angle of attack (PARB)	12.13°	Reynolds number	908579

It has to be noted that the springs in the FSI simulations were defined at respective degrees of freedom at its nodes. Hence no differences occur whether the simulations are performed with all springs connected to the foil or whether the simulations (y-directions, z-direction, x-rotation) are performed individually as long as the rigid body modes are always suppressed by the springs or boundary conditions. Fig. 62 shows the FSI results of segment 16 under the given loading and boundary conditions. The coupling effects of blade section 8 and 16 are presented in table xx. It shows that the deformation of the designed PARB will actually result in a reverse deformation of 0.24% at the outer blade segment. The amount of reverse deformation of the blade segments has to be considered in the design procedure of the PARB.

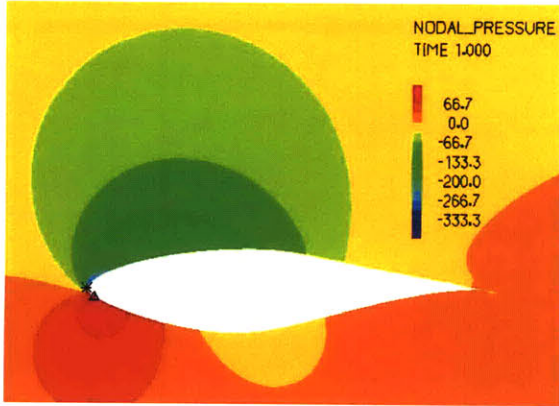


Fig. 61: Fluid flow in FSI simulation

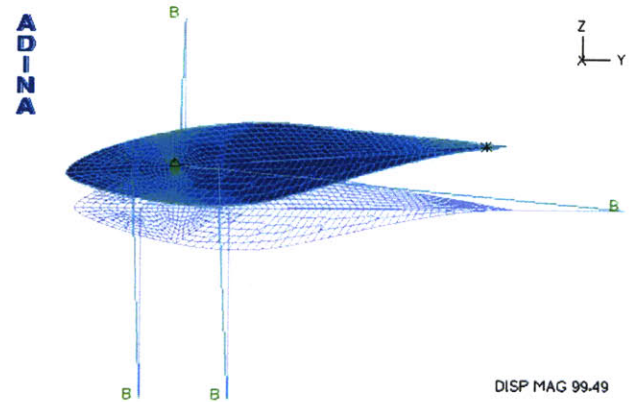


Fig. 62: Structural behavior in FSI simulation

Table 18: Impact of FSI coupling effects on blade deformations

Blade Segment	Deformation (twist angle) at wind speed = 9 [m/s]			
	Standard blade (# 6)	Ideal PARB	Optimized PARB (# 11)	Optimized PARB (# 11) + FSI correction [% of optimized PARB]
8	7.949°	-5°	-0.529°	99.8550%
16	17.472°	-9°	-0.751°	99.7645%

8.4. Discussion of the results

There are two possibilities to improve wind turbines by using passively adaptive rotor blades. One is to improve stall mechanisms which permit larger rotors due to a load reduction at higher wind velocities. The other option is to enhance the rotor's power efficiency. It strongly depends on the turbine type and its operating conditions, which option (1) or option (2) or neither of them has the potential to improve the turbine. For the case of enhancing the rotor's efficiency, a design procedure has been developed (Fig. 12) and it has been applied to improve the NREL phase VI wind turbine. The results show that a power enhancement is possible if the blade could adapt its shape nonlinearly by twisting. The necessary deformation of the optimal blade implies that a fully, passively adaptive blade is hardly feasible and one has to accept to only approach the ideal deformation. However, an adaptive blade in addition to a pitch control mechanism is physically

realistic and is able to capture the total improvement potential (3% - 6% in the case of the phase VI turbine).

The process we follow is to rotate the complete blade towards feather to a certain angular degree using a pitch mechanism. However this results into a too strong rotation towards the outer part of the blade. Therefore the passively adaptive rotor blade aims to twist the outer part back towards stall.

Structural dynamic analyses (ADINA), incorporating the simulation of composite materials (LAMICENS) provide deformation results for different rotor designs and materials. For a standard blade profile (constant thickness, isotropic material) aerodynamic loading during turbine operation leads at segment 16 to a twist of 17.5° towards feather, the power downgrading direction. Due to a systematic optimization of the structure, the developed PARB is able to generate a twist of 18.25° (segment 16) towards stall, the power upgrading direction.

The blade deformation however changes the aerodynamic loading onto the blade which has to be considered in the design process. This influence was analyzed in a coupled FSI simulation. In the case of the phase VI turbine, the FSI coupling results in a 0.24° reverse twisting (segment 16). This deformation is small but it is quite likely that this twist is larger for different turbine designs. The FSI correction loop is a necessary part of the comprehensive PARB design procedure.

9. Conclusion and outlook

The current worldwide energy system is fundamentally illogical and unsustainable. It depends to 85% on carbon based fossil fuels.

Driven by concerns on climate change, the finite nature of fossil fuels and the possibility to design scientifically more logical conversion processes, power generation technologies based on solar energy conversion or based on fluid flow conversion (e.g. hydro, wind, waves, tidal) will prevail in future energy systems.

Solar energy conversion devices will not reach cost parity with currently fossil fuel based power plants in the coming decade, but photovoltaic cells face a bright long-term future [6].

Fluid flow energy conversion is currently based on quite mature turbine technology. Innovative fluid flow energy conversion systems based on aero-elastic flutter or high-altitude wind energy

conversion systems using kites, could be possible long-term alternatives to replace classical turbine technologies.

For the mid-term perspective it has been found that passively adaptive rotor blades for horizontal-axis wind turbines have a high potential to improve wind turbines and hence provides a promising contribution possibility towards a sustainable energy supply.

Since aero-elastic effects are almost unavoidable in flexible blade designs. It is desirable to tailor these effects to our advantage by a controlled use of orthotropic material properties and a smart design of the blade structure.

For this purpose a numerical procedure for the design of passively adaptive wind turbine blades has been developed. The optimization of the NREL phase VI turbine shows a possible ideal improvement potential of 3% to 6% for this turbine. Using current material technology the ideal deformation can not be fully achieved. However, the performed structural and material design optimization results in an effective improvement compared to standard blades.

For the design of commercially mature, passively adaptive rotor blades further research has to be conducted to improve the accuracy of simulation and design tools. Since minor changes in blade deformation have strong effects on the turbine's power output or the aerodynamic loads, a replacement of the BEMT code with a validated 3D CFD code will improve the simulation accuracy. Furthermore it has been shown that the design of passively adaptive rotor blades is a coupled problem and hence a direct 3D FSI coupling of FEM structural dynamic simulations and aerodynamic CFD simulations will further enhance the comprehensive design procedure.

Appendix A. Comparison of wind turbine simulation codes

Table A1: Participants and modeling codes used in the benchmark [74]

Participant	Organization	Code Name	Code Type	Code Description
Michael Selig	University of Illinois	PROPID-C	Performance	Performance model with BEM and Corrizan stall delay model
Philippe Giguere	Tech Univ of Denmark/	PROPID-UI	Performance	Performance model with BEM and UTOC stall delay model
Martin Hansen Takis	CRES Greece	ROT/ABEM	Performance	Performance model with BEM using 3-D corrected airfoil data based on a quasi-3D Navier-Stokes solver
Chaviaropoulos	Global Energy Concepts	ADAMS	Aeroelastic	Multi-body aeroelastic model using "AeroDyn" aerodynamics (BEM/Leishman-Beddoes)
David Malcolm, Tim McCov, Davrou Griffin	Loughborough University CREST UK	YAWDYN	Aeroelastic	Aeroelastic model with rigid blade flapping hinge blade using "AeroDyn" aerodynamics (BEM/Leishman-Beddoes)
James Shawler	Windward Engineering	ADAMS-1	Aeroelastic	Multi-body aeroelastic model using "AeroDyn" aerodynamics (equilibrium wake, BEM/Leishman-Beddoes)
Craig Hansen, Dave Latino		ADAMS-2	Aeroelastic	Same except "AeroDyn" with dynamic inflow, BEM/Leishman-Beddoes
		ADAMS-3	Aeroelastic	Same except "AeroDyn" with dynamic inflow and delayed stall, BEM/Leishman-Beddoes
Robert Rawlinson - Smith	Garrad-Hassan	BLADED	Aeroelastic	Assumed modes aeroelastic model with BEM/Beddoes-Leishman aerodynamics
Wayne Johnson	NASA Ames	Camrad II	Aeroelastic	Aero-mechanical rotorcraft analysis tool
Helge Madsen	Risoe	HawC	Aeroelastic	Aeroelastic model with BEM theory
		HawC-3D	Wake	Aeroelastic model with 3D CFD actuator disc model
Herman Snel, Koert Lindenburg	ECN	PHATAS	Aeroelastic	Aeroelastic model with BEM theory
Bjorn Montgomerie, Anders Bjarck, Hans Ganander	FFA/ Nordic Windpower/ Teknikeruppen	VIDYN	Aeroelastic	Aeroelastic code with "AerForce" aerodynamics and "DvnStall" dynamic stall (BEM/Leishman-Beddoes)
Niels Sorensen	Risoe	EllipSys3D	CFD	3D incompressible Navier-Stokes model
Robert Mikkelsen	Tech Univ. of Denmark	ADDWANS	CFD	Combined Navier-Stokes BEM approach
Lakshmi Sankar	Georgia Tech	Hybrid CFD	CFD	3D multi-domain analysis unsteady Navier-Stokes model
Guanpeng Xu		GENUVP	Wake	Vortex element, free wake model
Michael Belessis	CRES-NTUA	HawtDawg	Wake	Prescribed wake model (Horizontal Axis Wind Turbine Directly Allocated Wake Geometry)
Spyros Voutsinas	University of Glasgow		Wake	
Frank Coron, Tongguang Wang, Roddy Galbraith	Tech. Univ. of Delft	PREDICDYN	Wake	Asymptotic acceleration potential model
Gerard Van Bussel	CRES-NTUA	NS3D	Wake	3D steady RANS finite volume formulation, Chimera mesh
Michael Belessis				
Spyros Voutsinas				

References

- [1] GE Wind Energy, LLC, "Advanced Wind Turbine Program Next Generation Turbine Development Project," Subcontract Report NREL/SR-5000-38752, May 2006.
- [2] Tester JW, Drake, E, Driscoll, M, Golay, M, Peters, W. Sustainable Energy: Choosing Among Options. Cambridge, Mass: MIT Press, 2005.
- [3] Yang M, Blyth W, Bradley R, Bunn D, Clarke C, Wilson, T. Evaluating the power investment options with uncertainty in climate change policy. *Energy Economics* 2008;30(4):1933-1950.
- [4] Lior N, Energy resources and use: The present situation and possible paths to the future. *Energy* 2008;33(6):842-857.
- [5] Goldemberg J. World Energy Assessment, Energy and the Challenge of Sustainability. New York: United Nations Development Programme, United Nations Department of Economic and Social Affairs, 2001.
- [6] Deilmann C, Bathe KJ. A holistic method to design an optimized energy scenario and quantitatively evaluate promising technologies for implementation. *International Journal of Green Energy* 2009; 6: 1-21.
- [7] Burton T, Sharpe D. Wind Energy Handbook. John Willey & Sons, West Sussex, UK, 2001.
- [8] Bianchi F, Battista H, Mantz R. Wind Turbine Control Systems. Springer, London, UK, 2007.
- [9] Glauert H. Airplane propellers, aerodynamic theory. Springer Verlag, Berlin, 1935.
- [10] Glauert H. The elements of aerofoil and airscrew theory. Cambridge University press, Cambridge, England 1948.
- [11] Sengupta A, Verma MP. An analytical expression for the power coefficient of an ideal horizontal-axis wind turbine. *International Journal of Energy Research*, 16, 453-456.
- [12] Manwell J, McGowan JG. Wind energy explained. New York: John Wiley and sons Inc., 2002.
- [13] Hau E. Wind Turbines, Fundamentals, Technologies, Application. Springer, Heidelberg, Germany, 2006.
- [14] Abott H, Doenhoff AE. Theory of wing sections, including a summary of airfoil data. New York: Dover Publications, 1959.

-
- [15] Wilson RE, Lissamann PB, Walker SN. Applied aerodynamics of wind power machine. Oregon state university, 1974
- [16] Simms D, Schreck S, Hand M, Fingersh LJ. NREL Unsteady Aerodynamics Experiment in the NASA-Ames Wind Tunnel: A Comparison of Predictions to Measurements. Report no. NREL/TP-500-29494. Golden, CO: National Renewable Energy Laboratory, 2001.
- [17] Veers P, Bir G, Lobitz D. Aeroelastic tailoring in wind-turbine blade applications. Windpower '98, American Wind Energy Association Meeting and Exhibition, Bakersfield, California, April 28, 1998.
- [18] Lee AT, Flay RG. Compliant blades for wind turbines. IPENZ 1999;(26):7-12.
- [19] Lobitz D, Veers P, Eisler R. The use of twist-coupled blades to enhance the performance of wind turbines, report no. SAND2001-1303. Oak Ridge, TN: SANDIA Laboratory, U.S. Department of Energy, 2001.
- [20] Fingersh LJ, Carlin PW. Results from the NREL variable-speed test bed. ASME 17th Wind Energy Symposium, Reno, Nevada. January 12–15, 1998.
- [21] Du, Z. and Selig, M.S., "A 3-D Stall-Delay Model for Horizontal Axis Wind Turbine Performance Prediction," ASME/AIAA Joint Wind Energy Symposium, AIAA Paper 98-0021, Reno, NV, January 1998.
- [22] Cheng TH, Oh IK. Fluid-structure Coupled Analysis of Composite Wind Turbine Blades. Advanced Material Research 2007;25(28):41-44.
- [23] Gürdal Z, Haftka RT, Hajela Prabhat. Design and Optimization of Laminated Composite Materials. New York: John Willey and Sons Inc., 1999.
- [24] ADINA Theory and Modelling Guide Volume I: ADINA, November 2006, ADINA R&D, Inc. 71 Elton Avenue Watertown, MA 02472 USA.
- [25] Somers DM. Design and Experimental Results for the S809 Airfoil, Report no. NREL/SR-440-6918. Golden, CO: National Renewable Energy Laboratory 1997.
- [26] Bertagnolio F, Soerensen N, Johansen J, Fuglsang P. Wind Turbine Airfoil Catalogue. Report no. Risoe –R1280(EN). Roskilde, Denmark: Risoe National Laboratory, 2001.
- [27] Tangler JL. The Nebulous Art of Using Wind Tunnel Aerofoil Data for Predicting Rotor Performance. Wind Energy 2002;5:245-257.
- [28] Simms D, Schreck S, Hand M, Fingersh LJ. NREL Unsteady Aerodynamics Experiment in the NASA-Ames Wind Tunnel: A Comparison of Predictions to Measurements. Report no. NREL/TP-500-29494. Golden, CO: National Renewable Energy Laboratory, 2001.